Masterarbeit

Investigation of topology-driven magnetic reconnection with CWENO finite volume numerics

Freie Universität Berlin
Fachbereich Physik

Raquel Maya Mäusle

Betreuer: Prof. Dr. Wolf-Christian Müller (TU Berlin)
Zweitgutachter: Prof. Dr. Dieter Breitschwerdt (TU Berlin)

Abstract

Magnetic reconnection is a process in a plasma that changes the magnetic field topology due to finite electrical resistivity in the field's plasma environment. A possible trigger for the onset of reconnection is a high entanglement of the field lines which can exponentially amplify the influence of small resistive effects. This type of topology-driven reconnection is investigated by direct numerical simulations based on finite-volume numerics, in which the plasma is described by the ideal magnetohydrodynamic (MHD) equations. Numerical dissipation is utilized as a proxy of viscous and resistive non-idealities. A simple numerical configuration is used to study the relation of potential reconnection events and field line entanglement.

The application of an external velocity field induces magnetic field line movement through the frozen-in condition. It is used to drive the field lines of an initially homogeneous magnetic field with constant mean value pointing in the z-direction to a high degree of entanglement. The footpoints of the field lines are fixed at the boundaries in the z-direction, such that reconnection events can be observed by changes in the footpoint mapping from one z-boundary to the other. Damping layers at these boundaries are included in order to damp any perturbations caused by Alfvén waves propagating along the field lines. The boundary conditions orthogonal to the z-direction of the box-shaped simulation volume are periodic. In this configuration the system initially relaxes into a stationary state, in which the forces acting on the plasma balance each other and the field lines settle into a twisted state. This state of force-balance is spontaneously disrupted and a fast transition from the stationary state to a chaotic state is observed, which is accompanied by a sudden increase in both kinetic and magnetic energy. The influence of the grid resolution, the forcing amplitude and the damping coefficient is investigated and discussed.

The chaotic phase is further investigated and shown to be characterized by locally enhanced current densities, large separations of neighboring field lines and a change in the mapping of footpoints of particular field line bundles. The correlation of two key diagnostics is used to investigate the proposed connection between high entanglement and reconnection: the exponentiation number, σ_{max}, which quantifies the separation of field lines and which is a measure of the degree of entanglement, and the foot point velocity, v_{fp}, which is an indicator for potential reconnection events. It is shown that these two quantities are indeed temporally correlated, supporting the proposed theory. Furthermore, individual field lines undergo distinct reconnection events which happen on sub-Alfvénic timescales and which are correlated with high footpoint velocities. The abruptness of the events suggests that it is reconnection rather than resistive diffusion that causes the motion of the field lines.

Kurzzusammenfassung

Magnetische Rekonnektion ist ein Prozess in einem Plasma, bei dem sich die Topologie des Magnetfeldes durch die endliche elektrische Resistivität des ionisierten Mediums ändert. Ein möglicher Auslöser für Rekonnektion ist eine starke Deformation der Magnetfeldstruktur, welche den Einfluss kleiner resistiver Nichtidealitäten exponentiell verstärken kann. Diese Art der topologie-getriebenen Rekonnektion wird durch direkte numerische Finite-Volumen-Simulationen untersucht, in denen das Plasma mit Hilfe der idealen magnetohydrodynamischen (MHD) Gleichungen beschrieben wird. Anstelle von physikalischer Viskosität und Resistivität wird numerische Dissipation für die erforderlichen nicht-idealen Effekte verwendet. Der Zusammenhang zwischen Rekonnektion und der Deformation der Magnetfeldlinien wird mithilfe eines einfach aufgebauten numerischen Experiments untersucht.

Ein externes Kraftfeld wird verwendet um die Feldlinien des zu Beginn räumlich homogenen Magnetfelds in z-Richtung komplex zu verformen. Die Fußpunkte der Feldlinien werden an den Rändern des quaderförmigen Simulationsvolumens fixiert, sodass Rekonnektionsereignisse über die Veränderung der den jeweiligen Magnetfeldlinien zugeordneten Fußpunkten festgestellt werden können. Dämpfungsschichten an den Rändern in z-Richtung sorgen dafür, dass Störungen durch sich entlang des Magnetfeldes ausbreitende Alfvénwellen gedämpft werden. In x und y-Richtung sind die Randbedingungen periodisch. In dieser Konfiguration relaxiert das System in einen stationären Zustand, in dem die Kräfte, die auf das Plasma wirken, einander ausgleichen, die magnetischen Feldlinien derformiert sind und das Plasma annähernd ruht. Dieses Kräftegleichgewicht wird spontan und abrupt verlassen und es wird ein schneller Übergang von dem Gleichgewichtszustand zu einem chaotischen und dynamisch fluktuierenden Plasmaverhalten beobachtet, in dem sowohl die kinetische als auch die magnetische Energie neue quasistationäre, von breitbandigen Störungen in Raum und Zeit charakterisierte Niveaus einnehmen. Der Einfluss der Gitterauflösung, der Amplitude der antreibenden Kraft und des Dämpfungskoeffizienten wird untersucht und diskutiert.

Es wird gezeigt, dass die chaotische Phase durch lokal erhöhte Stromdichten, Feldliniendeformation und Abweichungen der Fußpunktpositionen gekennzeichnet ist. Die Korrelation von zwei der zentralen Diagnostiken wird berechnet, um den vorhergesagten Zusammenhang zwischen Feldlinienverformung und Rekonnektion zu untersuchen. Diese sind die Exponentiationszahl, σ_{max}, welche die Abstandsänderung benachbarter Feldlinien quantifiziert, sowie die virtuelle Fußpunktgeschwindigkeit, v_{fp}, welche ein Indikator für mögliche Rekonnektionsereignisse ist. Es wird gezeigt, dass diese Größen zeitlich korreliert sind. Desweiteren wird beobachtet, dass einzelne Feldlinien zeitlich und räumlich separierbare diskrete Ereignisse auf sehr kurzen Zeitskalen durchlaufen. Diese abrupte Plötzlichkeit der Ereignisse deutet darauf hin, dass diese durch Rekonnektion statt durch resistive Diffusion hervorgerufen wird.

Contents

1 Introduction

A plasma is a quasi-neutral ionized gas. It consists of charged particles interacting with self-generated magnetic and electric fields and it typically has a high electrical conductivity. Most of the visible matter in the universe is in a plasma state. Under certain conditions, a plasma can be described as a single fluid governed by the magnetohydrodynamic (MHD) equations. In astrophysical plasmas the evolution is often assumed to be ideal, corresponding to an infinite electric conductivity. In the ideal case the magnetic field is "frozen" into the plasma. This means that the field lines follow the motion of the plasma and cannot diffuse across it. The ideal limit is valid if the time scales of interest are much smaller than that of diffusion across any length scale of interest. Even when these conditions are met, resistivity can still be important when small scale structures appear, at which the assumption of ideality does not hold. In the presence of resistivity, the motion of the field lines is less constrained and they can diffuse across the plasma. The additional presence of strong gradients of the magnetic field can then even lead to a loss of field line integrity and the formation of a differently structured magnetic configuration. This process is called magnetic reconnection and it occurs in different types of plasmas. It is assumed to cause solar flares, auroral phenomena in the earth's magnetosphere as well as instabilities in fusion reactor devices. It is a process by which the connectivity of the magnetic field lines changes due to finite resistivity. This change in the magnetic topology is usually accompanied by a conversion of magnetic to kinetic energy [27].

The first MHD model to describe steady-state reconnection in a current sheet at a magnetic null point was developed by Sweet and Parker [31, 24]. In this two-dimensional model, a diffusion region lies between oppositely directed magnetic field lines, which form a so-called X-point. Incoming plasma flows push the magnetic field lines into this diffusion region, where they reconnect and are pushed outward, as shown in figure 1.1. However, the Sweet-Parker

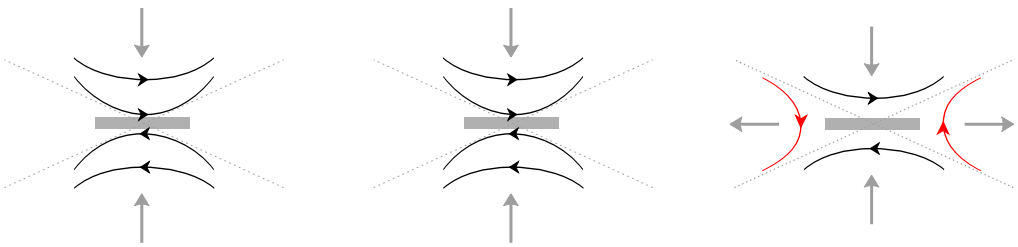

Figure 1.1: Schematic figure of the Sweet-Parker reconnection model: Oppositely directed magnetic field lines (black arrows) at an X-point are pushed towards each other by incoming plasma flow (gray arrows) and into a narrow diffusion region (shaded), in which they reconnect. The reconnected field lines (red arrows) are pushed outward.

model is referred to as a model for slow reconnection, as it cannot explain the fast time scales that are being observed in solar flares. Therefore many other models were developed with the aim of describing a faster reconnection process [27]. Often these models also describe reconnection in two dimensions. However, the behavior of field lines in three dimensions is fundamentally different, such that more recently investigations of magnetic reconnection have shifted focus to the three-dimensional case, see for example [16, 28, 25].

In this work a three-dimensional reconnection model is investigated, which is described in [10]. In this model, the proposed mechanism for reconnection is related to the entanglement of magnetic field lines. When these are driven to a high degree of entanglement, the field lines become exponentially sensitive to non-ideal effects. This means that a small resistive effect can trigger reconnection. This topology-driven reconnection model takes into consideration the behavior of neighboring magnetic field lines in three dimensions, from which a measure of the degree of entanglement can be obtained. A simple configuration is proposed in section II of [10], which is accessible to numerical investigation. It consists of an initially uniform magnetic field that is driven to high spatial complexity by an applied large-scale velocity forcing, which due to the frozen-in condition leads to field line motion. The relation between the degree of entanglement and the occurrence of magnetic reconnection can then be probed with this numerical experiment.

The aim of this work is to perform direct numerical simulations of the proposed model using a CWENO finite volume scheme to solve the ideal MHD equations. The non-ideal effects required for reconnection arise due to numerical dissipation. The setup requires special boundary conditions that keep the field lines fixed at the boundary. This makes it possible to keep track of individual field lines and thus offers a way of observing reconnection events in the simulation.

This work is structured as follows: chapter two provides the theoretical background on the fluid description of the plasma as well as on the magnetic reconnection model. In chapter three the numerical method is introduced and the specific requirements of the reconnection model such as the boundary conditions and the external forcing are described. The simulations and the post-processing of the data are described in chapter four and the simulation results are evaluated and discussed in chapter five. A summary and an outlook are given in chapter six.

2 Theoretical background

This chapter gives an overview of the theoretical background. The first part focuses on the plasma description using the *magnetohydrodynamic* (MHD) equations. A simple derivation of these equations and of their dimensionless form is shown, after which the frozen flux theorem, also known as Alfvén's theorem, is derived.

In the second part the concept of topology-driven magnetic reconnection is introduced and the behavior of magnetic field lines in three dimensions is discussed. Next, the numerical experiment for the investigation of this model is described. Finally, the concept of exponential sensitivity is introduced and the calculation of the exponentiation number, a characteristic quantity for field line behavior, is outlined.

2.1 Plasma description

A fully-ionized plasma is a quasi-neutral gas, consisting of electrons and one or multiple species of ions. The dynamics are governed by self-generated electric and magnetic fields, that affect and are affected by the motion of the charged particles. The forces these fields exert on the particles lead to a collective behavior of the plasma. A plasma can be described by different models of varying complexity. To completely and accurately describe its dynamics, the positions and velocities of all particles would have to be known. However, this is neither achievable with today's computational power nor practical, as one is generally interested in averaged quantities rather than the position and velocity of each particle. Commonly, either kinetic or fluid models are used instead. In a kinetic model, a statistical approach is used to describe the plasma. The development of the velocity distribution function for each point in space is considered. In a fluid model, the plasma is described as one or multiple conducting fluids. Instead of considering the distribution function at each point, macroscopic quantities such as the average density and velocity are used [5].

In this work a one-fluid model is used to describe the plasma. The governing equations are the MHD equations. They are a system of nonlinear partial differential equations, which determine the evolution of the density ρ, the velocity components (v_x, v_y, v_z), the plasma pressure p and the magnetic field components (B_x, B_y, B_z), giving a priori eight variables. This approximation works when studying slow and large scale dynamics of plasmas. It is applicable when the characteristic time and length scales of the system are much larger than those associated with collisions of the plasma particles, Debye screening and ion gyration [5].

2.1.1 Derivation of the MHD equations

The MHD equations can be derived from kinetic theory. For simplicity, a macroscopic derivation based on [7] is outlined here instead. It starts from the continuity equation, the gas' equation of state, Maxwell's equations and the forces acting on the plasma.

Mass is a conserved quantity and therefore the density, ρ, fulfills the continuity equation

$$\partial_t \rho + \boldsymbol{\nabla} \cdot (\rho \boldsymbol{v}) = 0 \tag{2.1}$$

$$\partial_t \rho + \boldsymbol{v} \cdot \boldsymbol{\nabla} \rho + \rho \boldsymbol{\nabla} \cdot \boldsymbol{v} = 0, \tag{2.2}$$

with $\partial_t \equiv \frac{\partial}{\partial t}$. This shows that any temporal change of ρ is associated with the flux of mass $\rho \boldsymbol{v}$. Using the convective derivative $\frac{\mathrm{d}}{\mathrm{d}t} \equiv \partial_t + \boldsymbol{v} \cdot \boldsymbol{\nabla}$ this can be rewritten as

$$\frac{\mathrm{d}\rho}{\mathrm{d}t} = -\rho \boldsymbol{\nabla} \cdot \boldsymbol{v}. \tag{2.3}$$

In the incompressible case the plasma density following the path of any fluid element is constant, $\frac{\mathrm{d}\rho}{\mathrm{d}t} = 0$. It follows that in this case the velocity field is divergence free, $\boldsymbol{\nabla} \cdot \boldsymbol{v} = 0$.

The momentum equation can be derived by considering the forces acting on a fluid element of volume δV. These are the following:

(a) The pressure force $-\delta V \boldsymbol{\nabla} p$ describes the force exerted on the fluid element due to the pressure gradient. Here it is assumed that the pressure is isotropic, such that the pressure tensor is reduced to the scalar pressure p.

(b) The Lorentz force acting on a fluid element, $\sum_i q_i \left(\boldsymbol{E} + \boldsymbol{v}_i \times \boldsymbol{B}\right)$, is the sum of forces acting on the particles of charge q_i due to the magnetic and electric field, $\boldsymbol{B}$ and $\boldsymbol{E}$, respectively. Rewriting this in terms of the net charge, δq, and the net current, $\delta \boldsymbol{j}$, of the fluid element leads to $\delta V \, \boldsymbol{j} \times \boldsymbol{B}$, as quasi-neutrality, i.e. the lack of fluctuations of the charge density on macroscopic spatial and temporal scales, results in $\delta q \simeq 0$.

(c) The viscous force is defined as $\delta V \boldsymbol{\nabla} \cdot \bar{\bar{S}}$, where $\bar{\bar{S}}$ is the viscous stress tensor. Its components are given by

$$\bar{\bar{S}}_{ij} = \mu \left(\partial_i v_j + \partial_j v_i - \frac{2}{3} \delta_{ij} \boldsymbol{\nabla} \cdot \boldsymbol{v} \right), \tag{2.4}$$

where μ is the dynamic viscosity and δ_{ij} is the Kronecker delta (equal to 1 if $i = j$ and 0 otherwise). In the incompressible case ($\boldsymbol{\nabla} \cdot v = 0$) the viscous force simplifies to

$$\boldsymbol{\nabla} \cdot \bar{\bar{S}} = \mu \boldsymbol{\nabla}^2 \boldsymbol{v}.$$

(d) Any additional body force acting on the fluid element can be written as $\delta V \boldsymbol{F}$, e.g. the gravitational force, which is, however, not relevant int the scope if this work.

Putting these terms together leads to the momentum equation

$$\rho \frac{\mathrm{d}\boldsymbol{v}}{\mathrm{d}t} = -\boldsymbol{\nabla} p + \boldsymbol{j} \times \boldsymbol{B} + \boldsymbol{\nabla} \cdot \bar{\bar{S}} + \boldsymbol{F}. \tag{2.5}$$

Expanding the convective derivative gives rise to the final expression for the momentum equation

$$\rho\partial_t \boldsymbol{v} = -\boldsymbol{v}\cdot\boldsymbol{\nabla}\boldsymbol{v} - \boldsymbol{\nabla}p + \boldsymbol{j}\times\boldsymbol{B} + \boldsymbol{\nabla}\cdot\bar{\bar{S}} + \boldsymbol{F}. \tag{2.6}$$

Next Maxwell's equations are used to find expressions for the current density, $\boldsymbol{j}$, and the magnetic field, $\boldsymbol{B}$. They are given by

Gauss's law	$\boldsymbol{\nabla}\cdot\boldsymbol{E} = \frac{\rho_{el}}{\epsilon_0} \simeq 0,$	(2.7)
Gauss's law for magnetism	$\boldsymbol{\nabla}\cdot\boldsymbol{B} = 0,$	(2.8)
Maxwell-Faraday equation	$\boldsymbol{\nabla}\times\boldsymbol{E} = -\partial_t\boldsymbol{B},$	(2.9)
Ampère's law	$\boldsymbol{\nabla}\times\boldsymbol{B} = \mu_0\boldsymbol{j},$	(2.10)

where in Ampére's law the displacement current can be neglected for non-relativistic plasma velocities. The Maxwell-Faraday equation describes the evolution of the magnetic field. Ampère's law determines the current density and can be used to expand the $\boldsymbol{j}\times\boldsymbol{B}$ term, giving

$$\boldsymbol{j}\times\boldsymbol{B} = -\boldsymbol{\nabla}\frac{B^2}{2\mu_0} + \frac{(\boldsymbol{B}\cdot\boldsymbol{\nabla})\boldsymbol{B}}{\mu_0}. \tag{2.11}$$

The two terms are associated with the magnetic pressure and the magnetic tension force, respectively. The latter is related to the curvature of the magnetic field lines and acts on straightening them.

Gauss's law cannot be used to determine the electric field as quasi-neutrality leads to a vanishing charge density, ρ_{el}. Instead, Ohm's law is used, which in the restframe of the fluid element is given by $\boldsymbol{E} = \eta_{el}\boldsymbol{j}$, with η_{el} the electrical resistivity. In the laboratory reference frame the fluid element is moving at the speed v. The electric field is therefore obtained by a Galilean transformation, $\boldsymbol{E} \to \boldsymbol{E}' = \boldsymbol{E} + \boldsymbol{v}\times\boldsymbol{B}$, which leads to the generalized version of Ohm's law

$$\boldsymbol{E}' = \boldsymbol{E} + \boldsymbol{v}\times\boldsymbol{B} = \eta_{el}\boldsymbol{j}, \tag{2.12}$$

where $\boldsymbol{E}$ is the electric field in the laboratory frame and $\boldsymbol{E}'$ is the electric field in the restframe of the fluid element. Using this in the Maxwell-Faraday equation leads to the induction equation, which governs the magnetic field evolution:

$$\begin{aligned}\partial_t\boldsymbol{B} &= \boldsymbol{\nabla}\times(\boldsymbol{v}\times\boldsymbol{B}) - \eta_{el}\boldsymbol{\nabla}\times\boldsymbol{j} \\ &= \boldsymbol{\nabla}\times(\boldsymbol{v}\times\boldsymbol{B}) - \frac{\eta_{el}}{\mu_0}\boldsymbol{\nabla}\times(\boldsymbol{\nabla}\times\boldsymbol{B}) \\ &= \boldsymbol{\nabla}\times(\boldsymbol{v}\times\boldsymbol{B}) + \eta\boldsymbol{\nabla}^2\boldsymbol{B}.\end{aligned} \tag{2.13}$$

Here the magnetic diffusivity, $\eta = \frac{\eta_{el}}{\mu_0}$, has been introduced.

In order to close the system of equations, the pressure p has to be determined from the equation of state, which in this work is taken to be isothermal. In this case the pressure is simply given by

$$p = \rho c_s^2, \tag{2.14}$$

where c_s is the sound speed, constant in the whole domain, due to the constancy of the temperature T for an isothermal system. The ideal gas law shows that for a constant temperature, the pressure only depends on the density:

$$\begin{aligned} p &= \frac{Nk_BT}{V} \\ &= \frac{Nk_BT}{m}\rho \\ &= R_s\,\rho T, \end{aligned} \tag{2.15}$$

where N is the number of molecules, k_B is the Boltzmann constant, V is the volume, m is the total mass and R_s is the specific gas constant. The density is given by $\rho = \frac{m}{V}$. Furthermore, the temperature of an ideal gas is related to its kinetic energy, $E_{kin} = \frac{3}{2}Nk_BT$, such that the pressure can be understood as kinetic energy per volume. The number of variables described by the MHD equations is thus reduced to seven in the isothermal case.

The closed system of MHD equations then consists of the following equations

$$\partial_t\rho = -\boldsymbol{\nabla}\cdot(\rho\boldsymbol{v}), \tag{2.16}$$

$$\rho\,\partial_t\boldsymbol{v} = -\rho(\boldsymbol{v}\cdot\boldsymbol{\nabla})\boldsymbol{v} - \boldsymbol{\nabla}p + \frac{1}{\mu_0}(\boldsymbol{\nabla}\times\boldsymbol{B})\times\boldsymbol{B} + \boldsymbol{\nabla}\cdot\bar{\bar{S}} + \boldsymbol{F}, \tag{2.17}$$

$$\partial_t\boldsymbol{B} = \boldsymbol{\nabla}\times(\boldsymbol{v}\times\boldsymbol{B}) + \eta\boldsymbol{\nabla}^2\boldsymbol{B}, \tag{2.18}$$

$$p = \rho c_s^2, \tag{2.19}$$

under the constraint $\boldsymbol{\nabla}\cdot B = 0$.

The ideal inviscid MHD equations are obtained from equations (2.16)-(2.19) by setting the viscosity term in the momentum equation and the magnetic diffusivity term (corresponding to the electrical resistivity) in the induction equation to zero. The relative importance of the viscous and resistive terms becomes apparent when the equations are transformed into a non-dimensional form. This is shown in the following section.

2.1.2 Non-dimensional equations

The MHD equations can be rewritten in a non-dimensional form by introducing characteristic scales for time and length, t_0 and L_0, as well as for the quantities $(\rho, \boldsymbol{v}, \boldsymbol{B})$. The temporal and spatial derivatives are then transformed to non-dimensional derivatives, $\partial t'$ and $\boldsymbol{\nabla}'$, by

$$\begin{aligned} \partial_t &\rightarrow \frac{1}{t_0}\partial_{t'} \\ \boldsymbol{\nabla} &\rightarrow \frac{1}{L_0}\boldsymbol{\nabla}'. \end{aligned} \tag{2.20}$$

The variables are written in terms of their characteristic scales (marked with subscript zero) and dimensionless quantities (marked with primes), e.g. $\rho \rightarrow \rho_0\rho'$.

Using this in equations (2.16)-(2.19) leads to

$$\begin{aligned}
\partial_{t'}\rho' &= -\boldsymbol{\nabla}' \cdot (\rho' \boldsymbol{v}'), \\
\rho' \, \partial_{t'} \boldsymbol{v}' &= -\rho'(\boldsymbol{v}' \cdot \boldsymbol{\nabla}')\boldsymbol{v}' - \frac{p_0}{\rho_0 v_0^2}\boldsymbol{\nabla}' p' + \frac{B_0^2}{\mu_0 \rho_0 v_0^2}(\boldsymbol{\nabla}' \times \boldsymbol{B}') \times \boldsymbol{B}' + \frac{\mu}{\rho_0 v_0 L_0}\boldsymbol{\nabla}' \cdot \bar{\bar{S}}' + \frac{F_0 L_0}{\rho_0 v_0^2}\boldsymbol{F}', \\
\partial_{t'} \boldsymbol{B}' &= \boldsymbol{\nabla}' \times (\boldsymbol{v}' \times \boldsymbol{B}') + \frac{\eta}{v_0 L_0}\boldsymbol{\nabla}'^2 \boldsymbol{B}',
\end{aligned} \tag{2.21}$$

where the relation $v_0 = \frac{L_0}{t_0}$ was used. The viscous stress tensor was rewritten as $\bar{\bar{S}} \to \mu v_0 / L_0 \bar{\bar{S}}'$ using equation (2.4). Evidently only terms in the momentum and induction equation contain coefficients due to the introduction of the non-dimensional variables. Therefore the choice of the remaining characteristic quantities, $\rho_0, L_0, t_0, p_0, B_0$ and F_0, as well as the viscosity, μ, and the magnetic diffusivity, η, determine the weight of the individual terms.

The characteristic pressure, p_0, only appears in front of the pressure gradient in the momentum equation. As stated above, pressure is related to the kinetic energy density. Therefore the characteristic pressure can be set to $p_0 = \rho_0 v_0^2$, such that the coefficient is equal to one. The characteristic external force can be written as $F_0 = \frac{\rho_0 v_0^2}{L_0}$, such that the prefactor of F' becomes one as well.

B_0 and ρ_0 are taken as the mean magnetic field strength and the mean density, and L_0 is defined as the box size of the system along the mean guide magnetic field. One can further set the characteristic velocity to the Alfvén velocity, $v_0 = v_A$, which is defined as $v_A = \sqrt{\frac{B_0^2}{\mu_0 \rho_0}}$. This choice means that the time is measured in Alfvén time units, such that $t_0 = t_A = L_0 / v_A$.

Only two coefficients remain: one determines the influence of viscosity and the other of magnetic diffusivity on the system. In both cases dimensionless quantities are introduced, namely the Reynolds number, R_e, and the magnetic Reynolds number, R_m, (which is equal to the Lundquist number since $v_0 = v_A$)[6]. They are defined as:

$$R_e \equiv \frac{\rho_0 v_0 L_0}{\mu}, \tag{2.22}$$

$$R_m \equiv \frac{v_0 L_0}{\eta}. \tag{2.23}$$

This finally leads to the non-dimensional set of equations (in which the primes are omitted):

$$\begin{aligned}
\partial_t \rho &= -\boldsymbol{\nabla} \cdot (\rho \boldsymbol{v}), \\
\rho \, \partial_t \boldsymbol{v} &= -\rho(\boldsymbol{v} \cdot \boldsymbol{\nabla})\boldsymbol{v} - \boldsymbol{\nabla} p + (\boldsymbol{\nabla} \times \boldsymbol{B}) \times \boldsymbol{B} + \frac{1}{R_e}\boldsymbol{\nabla} \cdot \bar{\bar{S}} + \boldsymbol{F}, \\
\partial_t \boldsymbol{B} &= \boldsymbol{\nabla} \times (\boldsymbol{v} \times \boldsymbol{B}) + \frac{1}{R_m}\boldsymbol{\nabla}^2 \boldsymbol{B}.
\end{aligned} \tag{2.24}$$

The ideal MHD equations are obtained when R_m becomes infinite, corresponding to a plasma with infinite electrical conductivity. Similarly, the inviscid equations are obtained as the Reynolds number goes to infinity, such that the viscosity term in the momentum equation becomes negligible.

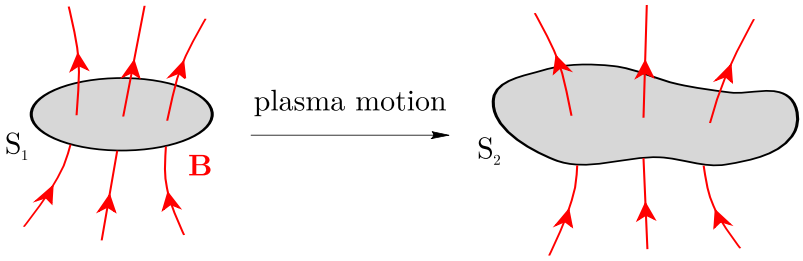

Figure 2.1: Schematic figure of the frozen flux theorem: in an ideal plasma the magnetic flux through a surface S is constant in time. When the surface is distorted by plasma motion, the field lines follow the motion, so that the flux through the surface (i.e. the number of field lines going through it) stays constant.

The numerical method used in this work solves the ideal, inviscid MHD equations. It can be used to study topology-driven magnetic reconnection, even though reconnection can only occur in the presence of non-ideal effects. This is due to the existence of numerical dissipation, which arises due to the discretization of the equations. It is essential for the numerical experiment carried out in this work, but has the disadvantage that its magnitude is not known or controllable.

2.1.3 Frozen flux theorem

In an ideal plasma the magnetic field lines are "frozen" into the plasma. This concept can be understood by considering an arbitrary, closed curve in space that is advected by the plasma. The magnetic flux through the surface defined by this curve is conserved. This means that as the curve is deformed by the plasma flow, the magnetic field lines passing through it are distorted as well.

This effect was first described by Hannes Alfvén and is thus known as Alfvéns theorem [1]. It can be derived from the expression for the magnetic flux, Φ_m, through a surface S defined by the closed curve C in an ideal plasma,

$$\Phi_m = \iint_S \boldsymbol{B} \cdot \mathrm{d}\boldsymbol{S}, \tag{2.25}$$

where $\mathrm{d}\boldsymbol{S}$ is the vector normal to an infinitesimal surface element. The change of magnetic flux over time can then be expressed as the sum of two terms,

$$\frac{\mathrm{d}\Phi_m}{\mathrm{d}t} = \iint_S \frac{\partial \boldsymbol{B}}{\partial t} \cdot \mathrm{d}\boldsymbol{S} + \oint_C \boldsymbol{B} \cdot (\boldsymbol{v} \times \mathrm{d}\boldsymbol{l}). \tag{2.26}$$

The first term describes the change in magnetic field, while the second one refers to a deformation of the surface, which is enclosed by the curve C. Changes to the surface can be expressed as $\boldsymbol{v} \times \mathrm{d}\boldsymbol{l}$, where $\boldsymbol{v}$ is the plasma velocity acting on the line element $\mathrm{d}\boldsymbol{l}$ and the closed line integral sums up all of these changes.

Substituting the ideal induction equation (2.13) into equation (2.26) then leads to

$$\begin{aligned}\frac{\mathrm{d}\Phi_m}{\mathrm{d}t} &= \iint_S \boldsymbol{\nabla} \times (\boldsymbol{v} \times \boldsymbol{B}) \cdot \mathrm{d}\boldsymbol{S} + \oint_C \boldsymbol{B} \cdot (\boldsymbol{v} \times \mathrm{d}\boldsymbol{l}) \\ &= \oint_C (\boldsymbol{v} \times \boldsymbol{B}) \cdot \mathrm{d}\boldsymbol{l} - \oint_C (\boldsymbol{v} \times \boldsymbol{B}) \cdot \mathrm{d}\boldsymbol{l} = 0,\end{aligned} \tag{2.27}$$

where in the second step Stokes's theorem was applied to the first term, so that both terms cancel each other out [27]. The magnetic flux in an ideal plasma is thus conserved in time, effectively freezing the magnetic field lines into the plasma. This is shown schematically in figure 2.1.

This property is important to understand the dynamics of the magnetic field lines, but also has a practical use when it comes to the numerical experiment presented in section 2.2.1. It can be used to fix the magnetic field lines at the bounding planes in z-direction by setting the velocity $\boldsymbol{v}$ at these boundaries to zero. As the magnetic field lines follow the plasma motion, this effectively prohibits them from moving at the boundaries, when the evolution is strictly ideal. In the presence of finite resistivity magnetic field line diffusion can lead to deviations from this ideal behavior.

2.2 Topology-driven magnetic reconnection

This section is based on Boozer's description of topology-driven magnetic reconnection, in which magnetic reconnection is discussed in three dimensions and a numerical experiment is proposed [10].

The following introduction to the theory is based on section I of [10], in which magnetic reconnection is defined as a process in which magnetic field lines change their connections, thereby changing the topology of the magnetic field. It can be shown that this can only occur when the evolution of the magnetic field deviates from an ideal evolution due to resistive effects. The demonstration involves the mathematical concept of generalized coordinates and is not included here.

Topology-driven magnetic reconnection can occur when the magnetic field is driven to a high spatial complexity. In the ideal case the magnetic field lines can be stretched and twisted and become increasingly entangled without ever being cut. However, the increasing spatial complexity of the magnetic field leads to an increased sensitivity to small non-ideal effects, a phenomenon that is characteristic of highly nonlinear systems and that is sometimes referred to as "butterfly effect". Specifically, this means that an exponentially small non-ideal effect can trigger reconnection in a highly entangled magnetic field. It is essential to study this in three dimensions in order to obtain high levels of entanglement, as a two-dimensional magnetic field is much more constrained.

A measure of the presence of non-ideal effects is obtained by integrating the electric field $\boldsymbol{E}$ along a magnetic field line

$$V \equiv \int \boldsymbol{E} \cdot \mathrm{d}\boldsymbol{l}, \tag{2.28}$$

which can be understood further by expressing the electric field with Ohm's law (eq. (2.12))

$$\boldsymbol{E} = \eta_{el}\boldsymbol{j} - \boldsymbol{v} \times \boldsymbol{B}. \tag{2.29}$$

Equation (2.28) then becomes

$$\begin{aligned} V &= \int (\eta_{el}\boldsymbol{j} - \boldsymbol{v} \times \boldsymbol{B}) \cdot \mathrm{d}\boldsymbol{l} \\ &= \int \eta_{el}\boldsymbol{j} \cdot \mathrm{d}\boldsymbol{l}, \end{aligned} \tag{2.30}$$

as $\boldsymbol{B}$ and $\mathrm{d}\boldsymbol{l}$ are parallel along a field line so that $(\boldsymbol{v} \times \boldsymbol{B}) \cdot \mathrm{d}\boldsymbol{l} = 0$. When the plasma is ideal it has an infinite electrical conductivity (that is $\eta_{el} = 0$), in which case equation (2.30) becomes $V = 0$. Conversely $V \neq 0$ indicates the presence of non-ideal effects. This measure is commonly used as a proxy for the reconnection rate [16, 15, 26].

To quantify the relative importance these non-ideal effects have on a certain magnetic field, the dimensionless parameter $\mathcal{B}$ is introduced as

$$\mathcal{B} \equiv \frac{\left|\int \boldsymbol{E} \cdot \mathrm{d}\boldsymbol{l}\right|}{E_0 L_0}, \tag{2.31}$$

where E_0 is the characteristic electric field strength and L_0 is a characteristic length scale of the system. This number gives an approximation of how much the non-ideal effects contribute to changes in the magnetic field. Using equations (2.30) and (2.10) and noting that the characteristic electric field strength is given by $E_0 = v_A B_0$ for a plasma with an Alfvénic $\boldsymbol{E} \times \boldsymbol{B}$ flow, equation (2.31) becomes:

$$\begin{aligned} \mathcal{B} &= \frac{\eta_{el}\left|\int \boldsymbol{\nabla} \times \boldsymbol{B} \cdot \mathrm{d}\boldsymbol{l}\right|}{\mu_0 v_A B_0 L_0} \\ &\approx \frac{\eta B_0}{v_A B_0 L_0} \\ &\approx \frac{1}{R_m}, \end{aligned} \tag{2.32}$$

showing that it is inversely related to the magnetic Reynolds number. Furthermore, the ratio of the two terms in the induction equation (2.13), which governs the evolution of the magnetic field, is given by

$$\begin{aligned} \frac{\left\|\boldsymbol{\nabla} \times (\boldsymbol{v} \times \boldsymbol{B})\right\|}{\left\|\eta \boldsymbol{\Delta} \boldsymbol{B}\right\|} &\approx \frac{L_0^2 v_A B_0}{\eta L_0 B_0} \\ &\approx R_m, \end{aligned} \tag{2.33}$$

which illustrates that the relative importance of the diffusive term is given by R_m, where again $v_0 = v_A$ is assumed. This means that non-ideal effects will influence the magnetic field evolution in proportion to $R_m^{-1} \approx \mathcal{B}$ on a time scale of the order of the Alfvén time $t_A = L_0/v_A$.

In astrophysical systems, $\mathcal{B}$ is usually of the order of 10^{-4} to 10^{-20}. It is commonly assumed that reconnection occurs when it increases to the order of unity, $\mathcal{B} \sim 1$, either due to sufficiently large current densities j (as $\mathcal{B} \sim j$) in small regions or through turbulence effects

[20]. For small $\mathcal{B}$ it is, however, more likely that reconnection is caused by entanglement, through which the field becomes exponentially sensitive to small non-ideal effects. In order to express this mathematically, the behavior of magnetic field lines has to be investigated. It can be shown that in three dimensions they tend to exponentiate apart, meaning that the distance between initially infinitesimally close magnetic field lines increases exponentially with the distance l along the field line. Denoting the separation between neighboring field lines at distance l along the lines by $\delta(l)$, this exponential behavior can be expressed as

$$\delta(l) = \delta_0 \, e^{\sigma(l)}, \tag{2.34}$$

where δ_0 is the initial separation and σ is the exponentiation number. It is a useful quantity to characterize the separation, which can vary across several orders of magnitude.

An increasingly complex and entangled magnetic field leads to increased current densities $\boldsymbol{j}$, as can be seen from the low-frequency Ampère's law in equation (2.10). Furthermore it can be shown that the maximum exponentiation number between field lines scales with the ratio of parallel current density to the characteristic current density of the system [9]

$$\sigma_{max} \sim \frac{j_{\parallel}}{B/(\mu_0 L)}, \tag{2.35}$$

such that σ_{max} is a measure of the entanglement of field lines.

As will be shown in section 2.2.2 the criterion for topology-driven reconnection can be written as

$$e^{\sigma_{max}} \mathcal{B} \sim 1, \tag{2.36}$$

which together with equation (2.35) gives rise to the current density, that is required to fulfill the criterion. It scales as

$$j_{\parallel} \sim \frac{B}{\mu_0 L} \ln\left(\frac{1}{\mathcal{B}}\right), \tag{2.37}$$

such that even in systems with small $\mathcal{B}$ the current density required for reconnection is comparably small.

In summary, $e^{\sigma_{max}} \mathcal{B} \sim 1$ has to be fulfilled for reconnection to occur. A magnetic field that is driven to high entanglement will lead to an increased current density, which results in a linear increase in $\mathcal{B}$ and an exponential growth through σ_{max}. In systems in which the characteristic value of $\mathcal{B}$ is much smaller than unity (e.g. space and astrophysical systems), the latter one is the dominant effect.

This theory of topology-driven magnetic reconnection can be investigated with the help of simulations. Before going into further detail on the exponential sensitivity and how to compute the exponentiation number, the numerical experiment proposed by Boozer is introduced.

2.2.1 Numerical experiment

A numerical model is proposed in section II of [10], which consists of a box-shaped computational domain, that is periodic in the x and y-directions with a period of length L_p. In the z-direction it is bounded by planes at $z = 0$ and $z = L$, which are assumed to be perfectly

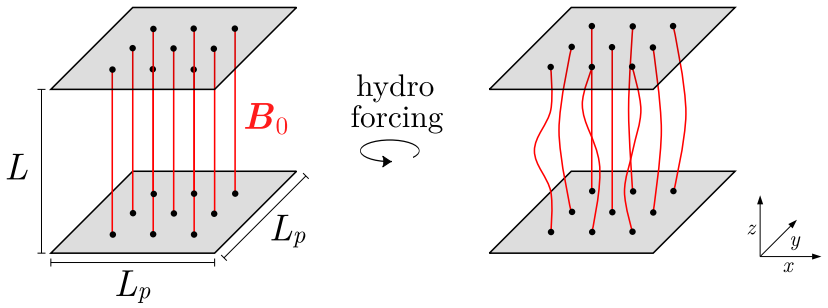

(a)

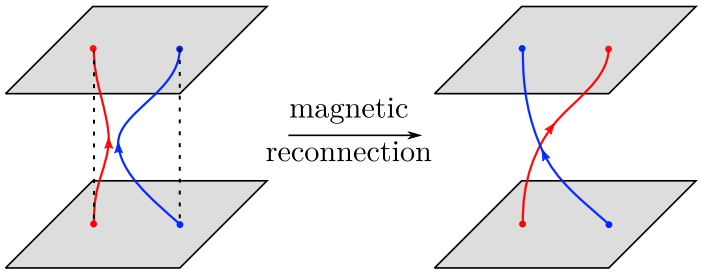

(b)

Figure 2.2: Numerical model for investigating reconnection: (a) the computational domain is periodic in x and y with a period of L_p and bounded by two perfectly conducting planes at $z = 0$ and $z = L$. At these planes the field lines are fixed and the mapping of footpoints from the bottom to top plane is trivial. The initial magnetic field $\boldsymbol{B}_0$ in the z-direction is driven into an entangled state by an applied forcing. (b) Magnetic reconnection changes the field line connections, which is visible through a change in the mapping of the footpoints.

conducting. The plasma is initially uniform and at rest with a uniform magnetic field that points in the z-direction, i.e.

$$\begin{aligned} \rho_0 &= 1, \\ (\rho \boldsymbol{v})_0 &= 0, \\ \boldsymbol{B}_0 &= B_0 \hat{\boldsymbol{z}}. \end{aligned} \tag{2.38}$$

As magnetic fields cannot move through a perfect conductor, the footpoints of the magnetic field lines are fixed at the two planes. This means that the field lines are free to move and stretch between the planes, but their footpoints cannot move across them, as shown schematically in figure 2.2a. This makes it possible to keep track of the individual field line identities while studying their dynamics between the planes. In order to achieve this behavior, special boundary conditions are necessary. As described in section 2.1.3, Alfvén's theorem states that in an ideal plasma the magnetic field lines follow the plasma movement. Therefore the footpoints of the field lines can be fixed by setting the plasma velocity at the boundary to zero, if the resistive effects due to numerical dissipation are sufficiently small.

Furthermore, this model can be used to study reconnection by observing changes in the field line connectivity. Each field line is defined by its coordinates (x_0, y_0) at the bottom plane, $z = 0$. The coordinates at the top plane are then a function of x_0, y_0 and time t and are denoted by $x_L(x_0, y_0, t)$ and $y_L(x_0, y_0, t)$. At $t = 0$ the mapping is trivial such that $x_L = x_0$ and

$y_L = y_0$ and it will stay so as long as the field lines' evolution is ideal. If magnetic reconnection occurs, there will be a change in the mapping, as illustrated in figure 2.2b. However, a change in the mapping does not necessarily mean that reconnection has occurred, but more generally indicates that the evolution has deviated from an ideal evolution, e.g. through field line diffusion.

A constant force field is applied to the plasma in order to entangle the magnetic field lines and drive reconnection. It should vanish at the z-boundaries, be periodic in the x and y-directions and have no component in the z-direction, such that field-parallel plasma dynamics are kept minimal. The following force field $\boldsymbol{F}$ and its corresponding driving potential U fulfill these requirements:

$$\boldsymbol{F} = \hat{\boldsymbol{z}} \times \boldsymbol{\nabla} U(x, y, z, t) \tag{2.39}$$

$$U = \pi \left(\frac{L_p}{L}\right)^2 \frac{B_0^2}{\mu_0 \rho_0} u(x, y, z, t), \tag{2.40}$$

where ρ_0 is the initial uniform density and u is a dimensionless potential, which is chosen as

$$u = (1 - e^{-t/\tau}) \left[\mathcal{S}(x, y) \sin\left(\frac{\pi z}{L}\right) + \mathcal{C}(x, y) \sin\left(\frac{2\pi z}{L}\right)\right] u_a \quad . \tag{2.41}$$

The forcing amplitude is regulated through the time constant τ and reaches a final amplitude of u_a. The dependence on x and y is contained in $\mathcal{S}$ and $\mathcal{C}$, which are defined as:

$$\begin{aligned} \mathcal{S}(x, y) &\equiv \sin\left(\frac{2\pi x}{L_p}\right) \sin\left(\frac{2\pi y}{L_p}\right) \\ \mathcal{C}(x, y) &\equiv \cos\left(\frac{2\pi x}{L_p}\right) \cos\left(\frac{2\pi y}{L_p}\right). \end{aligned} \tag{2.42}$$

The power put into the system by the forcing is $\boldsymbol{v} \cdot \boldsymbol{F}$ and is thus dependent on the plasma velocity $\boldsymbol{v}$. If the system relaxes into an equilibrium with no plasma flow, then the power input is also zero.

Furthermore, the relation between the exponentiation number and the applied forcing can be estimated by assuming that the system reaches a longterm quasi-stationary state in which $\rho \boldsymbol{F} \sim \boldsymbol{j} \times \boldsymbol{B}$. The derivation is presented in section IV B of [10] and is briefly outlined here.

In the strong guide field limit, $L/L_p \to \infty$, the magnetic field can be written as

$$\boldsymbol{B} = B_0 \hat{\boldsymbol{z}} + \boldsymbol{\nabla} A \times \hat{\boldsymbol{z}}, \tag{2.43}$$

where the scalar potential, $A(x, y, z, t)$, determines the magnetic field components perpendicular to the constant strong guide field given by $B_0 \hat{z}$. The current density in this case becomes

$$\boldsymbol{j} = \frac{1}{\mu_0} \boldsymbol{\nabla} \times \boldsymbol{B} = \frac{1}{\mu_0} \left(\boldsymbol{\nabla} \partial_z A - \hat{z} \nabla^2 A\right). \tag{2.44}$$

From equations (2.43)-(2.44) $\boldsymbol{j} \times \boldsymbol{B}$ can be expressed as

$$\boldsymbol{j} \times \boldsymbol{B} = -\frac{1}{\mu_0} \left(B_0 \hat{\boldsymbol{z}} \times \boldsymbol{\nabla} \partial_z A - \nabla_\perp^2 A \boldsymbol{\nabla} A\right), \tag{2.45}$$

where $\nabla_\perp$ denotes the x and y-components of the gradient. The scaling of this term can be estimated by expressing A as

$$A = \frac{L_p^2}{L} B_0 \mathcal{A}(x, y, z, t), \tag{2.46}$$

where the non-dimensional potential $\mathcal{A}(x, y, z, t)$ is a measure of the strength of the magnetic field deviation from the guide field along the z-direction. Furthermore, it can be shown that $\mathcal{A} \sim \sigma$, such that $A \sim \frac{L_p^2}{L} B_0 \sigma$. Using this in equation (2.45) the forcing required to reach a certain exponentiation number can be estimated to scale as

$$\rho \boldsymbol{F} \sim \boldsymbol{j} \times \boldsymbol{B} \sim \frac{B_0^2}{\mu_0 L} \frac{L_p}{L} \sigma^2, \tag{2.47}$$

where the ion density in the original expression has been replaced by the average density ρ. This estimated scaling can be tested by varying the forcing amplitude and observing the number of exponentiations reached, which is expected to approximately scale as $\sigma \sim \sqrt{F}$.

2.2.2 Exponential sensitivity

The mapping of the bottom to the top plane introduced in the previous section is helpful in understanding the concept of exponential sensitivity. For an ideal evolution this mapping will remain trivial. An exponentially small non-ideal deviation can lead to magnetic reconnection, when the field lines exponentiate away from each other in the region between those planes.

This can be expressed mathematically by introducing the field line coordinates at the mid-plane, $x_{L/2}$ and $y_{L/2}$, which depend on the lateral footpoint coordinates at a boundary plate, x_0, y_0 and t. The derivatives of the mapping from the bottom to the mid plane contain information on how far the field lines deviate from their original position in the x-y plane. The Jacobian matrix $\boldsymbol{J}_l$ contains these derivatives and can be written in terms of its Singular Value Decomposition (SVD) [33]

$$\boldsymbol{J}_l \equiv \begin{pmatrix} \frac{\partial x_{L/2}}{\partial x_0} & \frac{\partial x_{L/2}}{\partial y_0} \\ \frac{\partial y_{L/2}}{\partial x_0} & \frac{\partial y_{L/2}}{\partial y_0} \end{pmatrix} = \boldsymbol{U} \cdot \begin{pmatrix} e^{\sigma} & 0 \\ 0 & e^{-\sigma} \end{pmatrix} \cdot \boldsymbol{V}^{\dagger}. \tag{2.48}$$

Similar to an eigenvalue decomposition, a SVD decomposes a matrix into the product of three matrices, where $\boldsymbol{U}$ and $\boldsymbol{V}^{\dagger}$ are orthogonal matrices (i.e. $\boldsymbol{U}^T \boldsymbol{U} = \boldsymbol{I}$). The entries of the diagonal matrix are the singular values, which in this case correspond to the largest possible deviation from the initial coordinates (x_0, y_0) given by e^{σ}. When the mapping preserves area, the singular values are positive and the inverse of each other, which means that the Jacobian matrix has a determinant of one. Actually, not the area but the magnetic flux has to be preserved by the mapping (see frozen-in theorem in section 2.1.3). However, area and flux conservation are the same if the field strength is independent of position. This avoids the use of flux conserving Jacobian matrices which would lead to a more involved formulation of the problem [10]. The interested reader can refer to section VE of [8].

Similarly, a Jacobian matrix $\boldsymbol{J}_u$ can be defined for the mapping from the mid to the top plane. The chain rule implies that the Jacobian matrix for the entire regions is then given by the product of both the upper and lower region, $\boldsymbol{J}_{ul} = \boldsymbol{J}_u \cdot \boldsymbol{J}_l$. In the absence of non-ideal effects,

reconnection cannot occur and the mapping from the top to the bottom plane is trivial, such that $\boldsymbol{J}_{ul}$ is the identity matrix:

$$\boldsymbol{J}_{ul} \equiv \boldsymbol{J}_u \cdot \boldsymbol{J}_l = \begin{pmatrix} 1 & 0 \\ 0 & 1 \end{pmatrix} = \boldsymbol{V} \cdot \begin{pmatrix} 1 & 0 \\ 0 & 1 \end{pmatrix} \cdot \boldsymbol{V}^{\dagger}. \tag{2.49}$$

Using this relation, an expression for the matrix of the upper region can be derived for the non-reconnecting case:

$$\boldsymbol{J}_u = \boldsymbol{V} \cdot \begin{pmatrix} e^{-\sigma} & 0 \\ 0 & e^{\sigma} \end{pmatrix} \cdot \boldsymbol{U}^{\dagger}. \tag{2.50}$$

Introducing a small non-ideal effect Δ in the evolution, for instance in the upper half of the system, leads to a modified Jacobian J_u

$$\boldsymbol{J}_u = \boldsymbol{V} \cdot \begin{pmatrix} e^{-\sigma} & 0 \\ \Delta & e^{\sigma} \end{pmatrix} \cdot \boldsymbol{U}^{\dagger}, \tag{2.51}$$

which in turn affects the mapping across the entire region

$$\boldsymbol{J}_{ul} = \boldsymbol{V} \cdot \begin{pmatrix} 1 & 0 \\ \Delta e^{\sigma} & 1 \end{pmatrix} \cdot \boldsymbol{U}^{\dagger}. \tag{2.52}$$

The field line connections are scrambled when $\Delta e^{\sigma} \gtrsim 1$, as this gives a matrix that is far from the identity matrix which is obtained in the ideal case. A non-ideal perturbation Δ is of the order of magnitude of $\mathcal{B}$, as this measures the relative magnitude of the resistive term to the ideal term in the induction equation (see equations (2.32)-(2.33)). This gives rise to the criterion for reconnection of the previous section: $e^{\sigma_{max}} \mathcal{B} \sim 1$.

While the above demonstration is useful for understanding the concept of exponential sensitivity, it only considers the separation of magnetic field lines in the x and y-directions. This is a good assumption for systems with a strong mean field in the z-direction, but in general the separation of field lines has components in all three directions. When it comes to the explicit computation of the exponentiation number in the following section, the more general case is considered.

2.2.3 Computation of the exponentiation number

The number of exponentiations σ along a field line is an important quantity, that can be used to localize areas in which magnetic reconnection is likely to occur. First of all, this requires the knowledge of the field line coordinates itself. Along these coordinates, quantities such as σ can be computed through an SVD [9, 17].

The coordinates along a magnetic field line, $\boldsymbol{r}$, are determined by solving the following differential equation

$$\frac{\mathrm{d}\boldsymbol{r}(l)}{\mathrm{d}l} = \boldsymbol{b}(\boldsymbol{r}) \tag{2.53}$$

with the initial condition

$$\boldsymbol{r}(l = 0) = (x_0, y_0, z_0), \tag{2.54}$$

where l is the length along the magnetic field line and $\boldsymbol{b} = \frac{\boldsymbol{B}}{\|\boldsymbol{B}\|}$ is the normalized magnetic field. In the proposed model, the field lines are located between two plates in the z-direction, such that the coordinate in the z-direction is initially set to zero, $z_0 = 0$, and the field line is followed until it reaches the end plate at $z = L$.

The exponentiation number is a quantity connected to the distance between two neighboring field lines $\boldsymbol{r}_0$ and $\boldsymbol{r}$. Their separation can be written as $\boldsymbol{\delta} = \boldsymbol{r} - \boldsymbol{r}_0$. Using this in equation (2.53) gives rise to a differential equation for the separation along the field lines

$$\begin{aligned} \frac{\mathrm{d}(\boldsymbol{\delta} + \boldsymbol{r}_0)}{\mathrm{d}l} &= \boldsymbol{b}(\boldsymbol{\delta} + \boldsymbol{r}_0) \\ \frac{\mathrm{d}\boldsymbol{\delta}}{\mathrm{d}l} &= \boldsymbol{b}(\boldsymbol{\delta} + \boldsymbol{r}_0) - \frac{\mathrm{d}\boldsymbol{r}_0}{\mathrm{d}l} \\ \frac{\mathrm{d}\boldsymbol{\delta}}{\mathrm{d}l} &= \boldsymbol{b}(\boldsymbol{\delta} + \boldsymbol{r}_0) - \boldsymbol{b}(\boldsymbol{r}_0). \end{aligned} \tag{2.55}$$

In the limit of two infinitesimally close field lines, $\delta \to 0$, this becomes

$$\frac{\mathrm{d}\boldsymbol{\delta}}{\mathrm{d}l} = (\boldsymbol{\nabla}\boldsymbol{b})_{\boldsymbol{r}_0} \cdot \boldsymbol{\delta}, \tag{2.56}$$

where $\boldsymbol{\nabla}\boldsymbol{b}$ is the Jacobian matrix of the normalized magnetic field. This equation consists of three coupled differential equations for the three components of $\boldsymbol{\delta}$ and can be expanded to

$$\frac{\mathrm{d}}{\mathrm{d}l}\begin{pmatrix}\delta_x \\ \delta_y \\ \delta_z\end{pmatrix} = \begin{pmatrix}\partial_x b_x & \partial_y b_x & \partial_z b_x \\ \partial_x b_y & \partial_y b_y & \partial_z b_y \\ \partial_x b_z & \partial_y b_z & \partial_z b_z\end{pmatrix} \cdot \begin{pmatrix}\delta_x \\ \delta_y \\ \delta_z\end{pmatrix} = \boldsymbol{M}(l) \cdot \begin{pmatrix}\delta_x \\ \delta_y \\ \delta_z\end{pmatrix}, \tag{2.57}$$

where for clarity the Jacobian matrix for the field line $\boldsymbol{r}_0$ at length l is denoted by $\boldsymbol{M}(l)$.

The formal solution to this equation is

$$\begin{pmatrix}\delta_x \\ \delta_y \\ \delta_z\end{pmatrix} = \exp\left(\int_0^l \boldsymbol{M}(l')\,\mathrm{d}l'\right)\begin{pmatrix}\delta_x \\ \delta_y \\ \delta_z\end{pmatrix}_{l=0}. \tag{2.58}$$

However, instead of computing the exponential, $\boldsymbol{N}(l) = \exp\left(\int_0^l \boldsymbol{M}(l')\,\mathrm{d}l'\right)$, directly, which may be numerically unstable [17], it can be determined by the differential equation

$$\frac{\mathrm{d}\boldsymbol{N}}{\mathrm{d}l} = \boldsymbol{M}\boldsymbol{N}, \tag{2.59}$$

which can be verified by substituting the expression for $\boldsymbol{N}$ into this equation:

$$\begin{aligned} \frac{\mathrm{d}}{\mathrm{d}l}\exp\left(\int_0^l \boldsymbol{M}(l')\,\mathrm{d}l'\right) &= \exp\left(\int_0^l \boldsymbol{M}(l')\,\mathrm{d}l'\right)\frac{\mathrm{d}}{\mathrm{d}l}\int_0^l \boldsymbol{M}(l')\,\mathrm{d}l' \\ &= \boldsymbol{M}\boldsymbol{N}. \end{aligned}$$

To solve equation (2.58), the initial value, $\boldsymbol{N}(l = 0)$, is required. As the integral in the exponent is evaluated from 0 to l, the integral will give the null matrix for $l = 0$. The exponent of the

null matrix gives the identity matrix, so that

$$\boldsymbol{N}(l=0) = \begin{pmatrix} 1 & 0 & 0 \\ 0 & 1 & 0 \\ 0 & 0 & 1 \end{pmatrix}.$$

After obtaining $\boldsymbol{N}(l)$ as described above, it can be used in equation (2.58), which can be compactly written as

$$\begin{aligned} \boldsymbol{\delta}(l) &= \boldsymbol{N}(l)\, \boldsymbol{\delta}_0 \\ \frac{\boldsymbol{\delta}(l)}{\|\boldsymbol{\delta}_0\|} &= \boldsymbol{N}(l)\, \hat{\boldsymbol{\delta}}_0, \end{aligned} \tag{2.60}$$

where $\hat{\boldsymbol{\delta}}_0$ is the normalized initial separation vector. This equation describes a linear transformation of the set of initial vectors, $\boldsymbol{\delta}_0$, to the set of separation vectors, $\boldsymbol{\delta}(l)$. The exponentiation number is independent of the norm of the initial separation vector, $\|\boldsymbol{\delta}_0\|$, which can be seen from its definition:

$$\sigma(l) = \ln\left(\frac{\|\boldsymbol{\delta}_m(l)\|}{\|\boldsymbol{\delta}_0\|}\right). \tag{2.61}$$

Here $\boldsymbol{\delta}_m(l)$ is the separation vector of maximal length:

$$\frac{\|\boldsymbol{\delta}_m(l)\|}{\|\boldsymbol{\delta}_0\|} = \max\left\|\boldsymbol{N}(l)\, \hat{\boldsymbol{\delta}}_0\right\|, \tag{2.62}$$

where the maximum on the right-hand side was taken over all the normalized initial separation vectors $\hat{\boldsymbol{\delta}}_0$ on a sphere of radius one. Therefore one can set $\|\boldsymbol{\delta}_0\| = 1$ without loss of generality concerning the exponentiation number σ.

The problem of finding this maximal separation and thus the exponentiation number is essentially a singular value problem and can be solved by finding the SVD of the matrix $\boldsymbol{N}$, as described above. The meaning of the singular values can be understood by the geometrical interpretation of a SVD for a 3×3 matrix. The set of initial separation vectors form a sphere of radius one. By applying the linear operator $\boldsymbol{N}$ onto this set, the sphere is transformed to an ellipsoid, the semi-axes of which correspond to the singular values of $\boldsymbol{N}$. In this case, the SVD of $\boldsymbol{N}$ can be written as

$$\boldsymbol{N} = \boldsymbol{U} \cdot \begin{pmatrix} e^{\sigma_1} & 0 & 0 \\ 0 & e^{\sigma_2} & 0 \\ 0 & 0 & e^{\sigma_3} \end{pmatrix} \cdot \boldsymbol{V}^{\dagger}. \tag{2.63}$$

The largest singular value then corresponds to the maximal separation $\|\delta_m(l)\|$ and its logarithm gives the exponentiation number.

Finally, this results in values for σ for each step of size dl for a single field line. Performing this calculation for many field lines (each defined by their respective starting coordinates at $z = 0$) and finding the maximum exponentiation number σ_{max} along each field line provides a way to check for the occurrence of large separations. The field lines with high σ_{max} are then exponentially sensitive to non-ideal effects and are possible candidates for magnetic reconnection events. The exponentiation number and footpoint mapping of the field lines together thus are useful tools for identifying and localizing occurences of reconnection.

3 Numerical method

There are several different numerical approaches to solving differential equations, e.g. finite differences, finite elements or finite volume schemes. In this work a dimension-by-dimension fourth order accurate finite volume CWENO (centrally weighted essentially non-oscillatory) scheme is used, which is described in great detail in [35]. It consists of a fourth-order accurate finite volume scheme to compute the right-hand side of the ideal MHD equations, where a constrained transport technique is used for the magnetic field components. A fourth-order accurate strong stability preserving Runge-Kutta (SSPRK) method is employed for the time evolution. It is used mainly for simulations of astrophysical plasmas.

For this work the code was used to simulate the setup described in section 2.2.1 to investigate topology-driven magnetic reconnection. This model requires special boundary conditions to fix the footpoints of the magnetic field lines at the z-boundaries. In the other two directions periodic boundaries are used, which are the default setting in this code. The required non-periodic boundary conditions were implemented as part of this work. The following sections give an overview of the main steps of the numerical scheme before describing the implementation of the boundary conditions and the external forcing in more detail.

3.1 Finite volume scheme

In any numerical scheme the computational domain, $(x, y, z) \in [0, L_x] \times [0, L_y] \times [0, L_z]$, has to be discretized in a certain way. In a finite volume approach this is realized by dividing the domain into discrete cells, each containing a certain volume. In this case, we make use of a Cartesian grid with box-shaped cells and the uniform grid sizes, Δx, Δy and Δz, as shown in figure 3.1a. The total number of grid cells in each direction is given by N_x, N_y and N_z, such that for example the total number of cells in the x-direction is given by $N_x = \frac{L_x}{\Delta x}$.

The differential equations to be solved numerically are the ideal MHD equations, which were introduced in section 2.1.1. The hydrodynamic equations can be rewritten in a conservative, dimensionless form:

$$\partial_t \rho = -\boldsymbol{\nabla} \cdot (\rho \boldsymbol{v}) \,, \tag{3.1}$$

$$\partial_t (\rho \boldsymbol{v}) = -\boldsymbol{\nabla} \cdot \left[\rho \boldsymbol{v} \boldsymbol{v}^T + \left(p + \frac{1}{2} |\boldsymbol{B}|^2 \right) \mathbb{1} - \boldsymbol{B} \boldsymbol{B}^T \right] , \tag{3.2}$$

where $\mathbb{1}$ is the 3×3 identity matrix and $\boldsymbol{B}\boldsymbol{B}^T$ is a second-order tensor. As before ρ, $\boldsymbol{v}$, $\boldsymbol{B}$, $\boldsymbol{E}$ and p denote the plasma density, velocity, magnetic field, electric field and pressure, re-

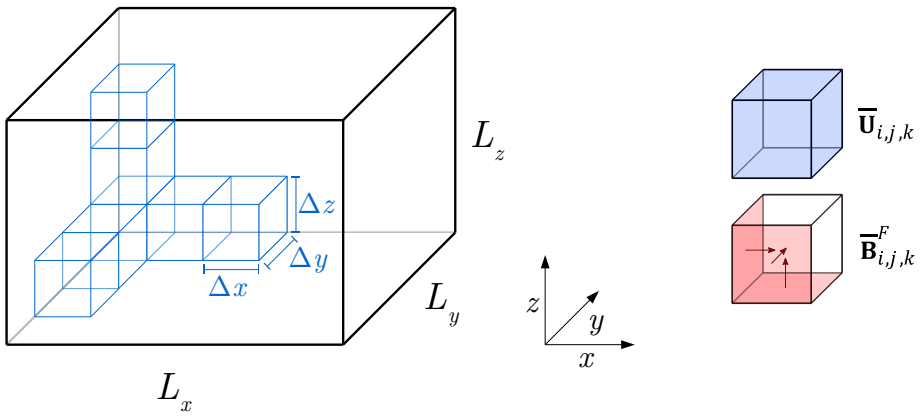

(a) *(b)*

Figure 3.1: Finite volume discretization: *(a)* the computational domain $(x, y, z) \in [0, L_x] \times [0, L_y] \times [0, L_z]$ is discretized into cells with grid sizes Δx, Δy and Δz. *(b)* In each of these cells the hydrodynamic variables are initially given as volume averages $\overline{\boldsymbol{U}}_{i,j,k}$ and the magnetic field components as face averages $\overline{B}^F_x$,$\overline{B}^F_y$ and $\overline{B}^F_z$ defined on the face normal to the respective component direction.

spectively. The conservative equations (3.1) – (3.2) imply that density and momentum of an arbitrary control volume only change by the respective flux densities across the control volume's surface. In the numerical finite-volume framework this translates to the exact mutual cancellation of flows across the boundary of any two neighboring grid cells. The conservation of these quantities is thus an inherent property of the finite-volume scheme.

The pressure is specified by the isothermal gas' equation of state (2.14). The magnetic field evolution is governed by the Maxwell-Faraday equation

$$\begin{aligned} \partial_t \boldsymbol{B} &= -\boldsymbol{\nabla} \times \boldsymbol{E} \\ &= \boldsymbol{\nabla} \times (\boldsymbol{v} \times \boldsymbol{B}). \end{aligned} \tag{3.3}$$

It should be noted that although these are the ideal MHD equations, diffusive effects exist due to numerical viscosity and resistivity, which are introduced by the discretization of the equations. While this type of diffusivity is not controllable and the magnitude unknown, it is essential for the numerical experiment carried out in this work, as reconnection can only occur in the presence of non-ideal effects.

Now the finite volume framework can be applied to the MHD equations. The hydrodynamic variables, $\boldsymbol{U} \equiv (\rho, \rho v_x, \rho v_y, \rho v_z)$, are evolved in time using equations (3.1)-(3.2). They are defined as volume averages $\overline{\boldsymbol{U}}_{i,j,k}$. The magnetic field components, $\boldsymbol{B} \equiv (B_x, B_y, B_z)$, are defined as staggered area averages $\overline{\boldsymbol{B}}^F_{i,j,k}$ on the corresponding faces of each cell as required by the constrained-transport procedure, e.g. B_x is defined on the face normal to the x-direction, as shown in figure 3.1b. Their evolution is described by equation (3.3).

3.1.1 Hydrodynamic variables

Mathematically, the cell average $\overline{\boldsymbol{U}}_{i,j,k}$ is obtained by integrating $\boldsymbol{U}$ over the cell volume:

$$\overline{\boldsymbol{U}}_{i,j,k} = \frac{1}{\Delta x \Delta y \Delta z} \iiint_{\Omega_{i,j,k}} \mathrm{d}x\,\mathrm{d}y\,\mathrm{d}z\,\boldsymbol{U}(x,y,z), \tag{3.4}$$

where $\Omega_{i,j,k}$ is the region of space spanned by $[x_i - \frac{\Delta x}{2}, x_i + \frac{\Delta x}{2}] \times [y_j - \frac{\Delta y}{2}, y_j + \frac{\Delta y}{2}] \times [z_k - \frac{\Delta z}{2}, z_k + \frac{\Delta z}{2}]$ and x_i, y_j and z_k are the coordinates of the central point of the cell (i,j,k), e.g. $x_i = (i + \frac{1}{2})\Delta x$.

Taking the time derivative of this equation and inserting equations (3.1)-(3.2) leads to

$$\begin{aligned} \frac{\mathrm{d}\overline{\boldsymbol{U}}_{i,j,k}}{\mathrm{d}t} &= \frac{1}{\Delta x \Delta y \Delta z} \iiint_{\Omega_{i,j,k}} \mathrm{d}x\,\mathrm{d}y\,\mathrm{d}z\,\frac{\mathrm{d}\boldsymbol{U}(x,y,z)}{\mathrm{d}t} \\ &= -\frac{1}{\Delta x \Delta y \Delta z} \iiint_{\Omega_{i,j,k}} \mathrm{d}x\,\mathrm{d}y\,\mathrm{d}z\,\boldsymbol{\nabla}\cdot\boldsymbol{f}, \end{aligned} \tag{3.5}$$

where $\boldsymbol{f}$ denotes the point-valued flux for each quantity in $\boldsymbol{U}$ that appears in the right-hand side of equations (3.1)-(3.2). With Gauss's theorem the volume integral is transformed into a surface integral over the surface S enclosing the volume with normal vector $\boldsymbol{n}$, giving

$$\begin{aligned} \frac{\mathrm{d}\overline{\boldsymbol{U}}_{i,j,k}}{\mathrm{d}t} &= -\frac{1}{\Delta x \Delta y \Delta z} \oiint_S \mathrm{d}S\,(\boldsymbol{f}\cdot\boldsymbol{n}) \\ &= -\frac{1}{\Delta x \Delta y \Delta z}\Bigg(\iint_{S_x} \mathrm{d}y\,\mathrm{d}z\,\left[\boldsymbol{f}^{\boldsymbol{x}}(x_{i+1/2},y,z) - \boldsymbol{f}^{\boldsymbol{x}}(x_{i-1/2},y,z)\right] \\ &\qquad + \iint_{S_y} \mathrm{d}x\,\mathrm{d}z\,\left[\boldsymbol{f}^{\boldsymbol{y}}(x,y_{j+1/2},z) - \boldsymbol{f}^{\boldsymbol{y}}(x,y_{j-1/2},z)\right] \\ &\qquad + \iint_{S_z} \mathrm{d}x\,\mathrm{d}y\,\left[\boldsymbol{f}^{\boldsymbol{z}}(x,y,z_{k+1/2}) - \boldsymbol{f}^{\boldsymbol{z}}(x,y,z_{k-1/2})\right]\Bigg), \end{aligned} \tag{3.6}$$

where the integration surfaces S_x, S_y and S_z are defined analogously to the volume $\Omega_{i,j,k}$, e.g. $S_x = [y_j - \frac{\Delta y}{2}, y_j + \frac{\Delta y}{2}] \times [z_k - \frac{\Delta z}{2}, z_k + \frac{\Delta z}{2}]$.

The x-component of the point-valued flux $\boldsymbol{f}^{\boldsymbol{x}}$ is defined at the center of the cell face normal to the x-direction and can be deduced from equations (3.1)-(3.2)

$$\boldsymbol{f}^{\boldsymbol{x}} = \begin{pmatrix} \rho v_x \\ \rho v_x^2 + p + \frac{1}{2}|\boldsymbol{B}|^2 - B_x^2 \\ \rho v_x v_y - B_x B_y \\ \rho v_x v_z - B_x B_z \end{pmatrix}. \tag{3.7}$$

Rewriting equation (3.6) in terms of area-averaged fluxes leads to

$$\frac{\mathrm{d}\overline{\boldsymbol{U}}_{i,j,k}}{\mathrm{d}t} = -\frac{\overline{\boldsymbol{F}}^{\boldsymbol{x}}_{i+1/2,j,k} - \overline{\boldsymbol{F}}^{\boldsymbol{x}}_{i-1/2,j,k}}{\Delta x} - \frac{\overline{\boldsymbol{F}}^{\boldsymbol{y}}_{i,j+1/2,k} - \overline{\boldsymbol{F}}^{\boldsymbol{y}}_{i,j-1/2,k}}{\Delta y} - \frac{\overline{\boldsymbol{F}}^{\boldsymbol{z}}_{i,j,k+1/2} - \overline{\boldsymbol{F}}^{\boldsymbol{z}}_{i,j,k-1/2}}{\Delta z}, \tag{3.8}$$

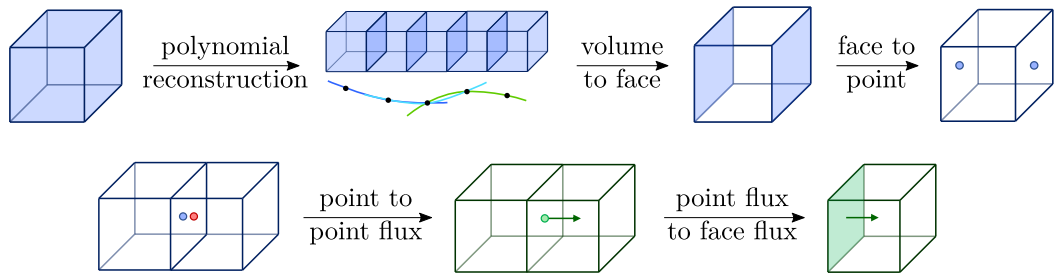

Figure 3.2: Main steps in the RHS computation of the hydrodynamic variables in one dimension: The initial cell averages are used to reconstruct the face averages with a CWENO polynomial reconstruction. After transforming the face averages to point values, the physical fluxes at each interface between two cells are computed and finally transformed into area-averaged fluxes.

with the area-averaged flux in the x-direction given by

$$\overline{\boldsymbol{F}}^{x}_{i\pm1/2,j,k} = \frac{1}{\Delta y \Delta z} \iint_{S_x} \mathrm{d}y\, \mathrm{d}z\; \boldsymbol{f}^{x}(x_{i\pm1/2}, y, z). \tag{3.9}$$

The fluxes in the y and z-direction are defined analogously.

Equation (3.8) is the final equation, from which the time evolution of the hydrodynamic variables can be obtained via time integration. This means that starting from initial cell averages, $\overline{\boldsymbol{U}}_{i,j,k}$, the area-averaged fluxes have to be calculated. This is done dimension by dimension, which spares computation time as compared to solving a truly multidimensional problem [34]. The main steps for the procedure in the x-direction are shown in figure 3.2, the first of which is described briefly below. Only a terse summary of the remaining steps is given. The reader interested in the technical details is kindly referred to section 3 of [35].

In the first step a 1D fourth-order polynomial is reconstructed from the cell-averaged values, which is centrally weighted and essentially non-oscillatory (CWENO). In order to achieve this behavior, three quadratic polynomials, $\boldsymbol{P}^{i}_{i-1,j,k}(x)$, $\boldsymbol{P}^{i}_{i,j,k}(x)$ and $\boldsymbol{P}^{i}_{i+1,j,k}(x)$, are reconstructed for each cell (i,j,k), using three cell averages each centered around the cells $i-1$, i and $i+1$, respectively. Therefore a total of five cells are needed, two to each side of the cell in which the polynomial is reconstructed. The coefficients of the polynomials are found uniquely through the conservation of the volume averages of the three cells being used, which can be written as

$$\begin{cases} \dfrac{1}{\Delta x} \displaystyle\int_{x_{m-3/2}}^{x_{m-1/2}} \mathrm{d}x\, \boldsymbol{P}^{i}_{m,j,k}(x) & = \overline{\boldsymbol{U}}_{m-1,j,k} \\ \dfrac{1}{\Delta x} \displaystyle\int_{x_{m-1/2}}^{x_{m+1/2}} \mathrm{d}x\, \boldsymbol{P}^{i}_{m,j,k}(x) & = \overline{\boldsymbol{U}}_{m,j,k} \\ \dfrac{1}{\Delta x} \displaystyle\int_{x_{m+1/2}}^{x_{m+3/2}} \mathrm{d}x\, \boldsymbol{P}^{i}_{m,j,k}(x) & = \overline{\boldsymbol{U}}_{m+1,j,k} \end{cases}, \tag{3.10}$$

with $m \in \{i-1, i, i+1\}$ denoting the three polynomials. These are then combined to give the final polynomial $\boldsymbol{R}_{i,j,k}(x)$ as

$$\boldsymbol{R}_{i,j,k}(x) = \sum_{m=i-1}^{i+1} w^{i}_{m,j,k} \boldsymbol{P}^{i}_{m,j,k}. \tag{3.11}$$

The weights $w^i_{m,j,k}$ are chosen to ensure fourth-order accuracy in smooth regions. In shocked regions, the polynomials corresponding to a discontinuity are associated with a vanishing weight, so as to prevent an oscillatory reconstruction. The weights are positive and sum up to one, such that the conservation constraint for $\boldsymbol{R}_{i,j,k}(x)$,

$$\frac{1}{\Delta x}\int_{x_{i-1/2}}^{x_{i+1/2}} \mathrm{d}x\, \boldsymbol{R}_{i,j,k}(x) = \overline{\boldsymbol{U}}_{i,j,k}, \tag{3.12}$$

is satisfied.

Next, area-averaged values are obtained by evaluating the reconstruction polynomial at $x_{i\pm1/2}$. These are converted to point values by means of a Taylor expansion, which are then used in equation (3.7) to compute the point-valued flux f^x. The passage through point values is necessary in order to keep the scheme fourth-order accurate. At each interface two fluxes are obtained, one from each cell at each side of the interface. Finding the physical flux at the interface is a Riemann problem, which is solved by employing the local Lax-Friedrichs flux (LLF) approximation. Finally, the point-valued physical flux is transformed into the area-averaged flux. These steps are repeated for the y and z-direction and the resulting area-averaged fluxes are used to compute the right-hand side of equation (3.8), after which the time integration is performed [35].

3.1.2 Magnetic field

Before describing the time integration method, however, the procedure for the magnetic field will be briefly outlined. It has to be treated separately in order to ensure $\boldsymbol{\nabla}\cdot B = 0$, which typically grows in time if the procedure used for the hydrodynamic variables is applied to the magnetic field components. Thus, in order to avoid unphysical effects, various different approaches can be employed. In this code the *constrained transport* (CT) procedure [14] is used, which maintains the solenoidality up to machine precision.

The magnetic field components are defined as area averages on the face normal to their respective direction, e.g. the x-component is given by

$$(\overline{B}^F_x)_{i-1/2,j,k} = \frac{1}{\Delta y \Delta z}\iint_{S_x} \mathrm{d}y\,\mathrm{d}z\; B_x(x_{i-1/2}, y, z), \tag{3.13}$$

where S_x refers to the cell surface with normal vector in the x-direction as used in equation (3.6). The y and z-components are defined analogously.

Taking the time derivative of equation (3.13) (and the corresponding equations for the y and z-components), using Faraday's law and applying Stokes's theorem results in

$$\frac{\mathrm{d}}{\mathrm{d}t}(\overline{B}^F_x)_{i-1/2,j,k} = -\frac{(\overline{E}_z)_{i-1/2,j+1/2,k} - (\overline{E}_z)_{i-1/2,j-1/2,k}}{\Delta y} + \frac{(\overline{E}_y)_{i-1/2,j,k+1/2} - (\overline{E}_y)_{i-1/2,j,k-1/2}}{\Delta z} \tag{3.14}$$

$$\frac{\mathrm{d}}{\mathrm{d}t}(\overline{B}^F_y)_{i,j-1/2,k} = -\frac{(\overline{E}_x)_{i,j-1/2,k+1/2} - (\overline{E}_x)_{i,j-1/2,k-1/2}}{\Delta z} + \frac{(\overline{E}_z)_{i+1/2,j-1/2,k} - (\overline{E}_z)_{i-1/2,j-1/2,k}}{\Delta x} \tag{3.15}$$

$$\frac{\mathrm{d}}{\mathrm{d}t}(\overline{B}_z^F)_{i,j,k-1/2} = -\frac{(\overline{E}_y)_{i+1/2,j,k-1/2} - (\overline{E}_y)_{i-1/2,j,k-1/2}}{\Delta x} + \frac{(\overline{E}_x)_{i,j+1/2,k-1/2} - (\overline{E}_x)_{i,j-1/2,k-1/2}}{\Delta y}, \tag{3.16}$$

where the electric field components encircling the surfaces are defined as edge-averaged values. The x-component is given by

$$(\overline{E}_x)_{i,j-1/2,k-1/2} = \frac{1}{\Delta x}\int_{x_{i-1/2}}^{x_{i+1/2}} \mathrm{d}x\ E_x(x, y_{j-1/2}, z_{k-1/2}). \tag{3.17}$$

It can be shown that this approach ensures the solenoidality of the magnetic field by considering the $\boldsymbol{\nabla}\cdot\boldsymbol{B}$ term, which can be approximated as

$$(\boldsymbol{\nabla}\cdot\boldsymbol{B})_{i,j,k} \approx \frac{(\overline{B}_x^F)_{i+1/2,j,k} - (\overline{B}_x^F)_{i-1/2,j,k}}{\Delta x} + \frac{(\overline{B}_y^F)_{i,j+1/2,k} - (\overline{B}_y^F)_{i,j-1/2,k}}{\Delta y} + \frac{(\overline{B}_z^F)_{i,j,k+1/2} - (\overline{B}_z^F)_{i,j,k-1/2}}{\Delta z}. \tag{3.18}$$

Inserting equations (3.14)-(3.16) into the time derivative of equation (3.18) leads to $\frac{\mathrm{d}}{\mathrm{d}t}(\boldsymbol{\nabla}\cdot\boldsymbol{B}) = 0$, as the terms cancel pairwise. Therefore the solenoidality is maintained at all times, as long as $\boldsymbol{\nabla}\cdot\boldsymbol{B}$ is zero initially.

Equations (3.14)-(3.16) determine the time evolution of the magnetic field from the edge-averaged electric field components, which have to be calculated from the initial area-averaged magnetic field and the reconstructed face-averaged velocity field. Once they are known, the equations can be integrated in time as described in the following section. As with the hydrodynamic variables, several steps are needed to compute the edge-averaged electric field component. The detailed descriptions and equations are not shown here. The interested reader is kindly referred to section 4 of [35].

3.2 Time integration

The time integration is done with a fourth-order strong stability-preserving Runge-Kutta (SSPRK) method, which avoids the introduction of oscillations due to the time integration. The method used in this code consists of ten stages and is described in section 6 of [35] and pseudocode 3 of [19]. The principle of the time integration is described for the classical four-stage Runge-Kutta (RK4) method, see for example [3], as this method is also used in the post-processing described in the following chapter.

Solving the MHD equations numerically is an initial value problem, that can be expressed as follows:

$$\frac{\mathrm{d}\boldsymbol{W}}{\mathrm{d}t} = \boldsymbol{C}[\boldsymbol{W}(t)], \quad \boldsymbol{W}(t_0) = \boldsymbol{W}_0. \tag{3.19}$$

Here the hydrodynamic variables and the magnetic field components are denoted as $\boldsymbol{W} = (\overline{\boldsymbol{U}}_{i,j,k}, \overline{\boldsymbol{B}}^F_{i,j,k})$, the right hand-sides of equations (3.8) and (3.14)-(3.16) as $\boldsymbol{C}[\boldsymbol{W}(t)]$ and the initial values as $\boldsymbol{W}_0$.

Now using a time step Δt, the value of $\boldsymbol{W}(t+\Delta t)$ can be approximated from the previous value $\boldsymbol{W}(t)$ as

$$\boldsymbol{W}(t+\Delta t) = \boldsymbol{W}(t) + \frac{1}{6}(\boldsymbol{k}_1 + 2\boldsymbol{k}_2 + 2\boldsymbol{k}_3 + \boldsymbol{k}_4), \tag{3.20}$$

where the quantities $\boldsymbol{k}_n, n \in \{1,2,3,4\}$ are defined as follows:

$$\begin{aligned}
\boldsymbol{k}_1 &= \Delta t\ \boldsymbol{C}\left[\boldsymbol{W}(t)\right] \\
\boldsymbol{k}_2 &= \Delta t\ \boldsymbol{C}\left[\boldsymbol{W}(t) + \frac{\boldsymbol{k}_1}{2}\right] \\
\boldsymbol{k}_3 &= \Delta t\ \boldsymbol{C}\left[\boldsymbol{W}(t) + \frac{\boldsymbol{k}_2}{2}\right] \\
\boldsymbol{k}_4 &= \Delta t\ \boldsymbol{C}\left[\boldsymbol{W}(t) + \boldsymbol{k}_3\right].
\end{aligned}$$

The time step is determined by the *Courant-Friedrichs-Lewy* (CFL) stability criterion [22]

$$\Delta t = C_{cfl} \min_{i,j,k} \left(\frac{\Delta x}{a^x_{i,j,k}}, \frac{\Delta y}{a^y_{i,j,k}}, \frac{\Delta z}{a^z_{i,j,k}} \right), \tag{3.21}$$

where C_{cfl} is the Courant number and $a^x_{i,j,k}$ is the local maximum speed of propagation of information in the x-direction, which corresponds to fast magnetosonic waves, see [35] for more details.. The time step is adapted for each iteration step for a more efficient computation. For a Courant number of one, the time step is given by the minimum time needed for information to propagate across a cell. The choice of the Courant number depends on the method used and its numerical stability. Due to the high stability of the SSPRK method used in this code, the Courant number is set to 1.95 for the 1D simulations and 1.5 for the 3D simulations presented in this work.

3.3 Boundary conditions

In any numerical simulation, the computational domain is finite and limited by its boundaries. It is therefore necessary to set boundary conditions that define what happens there.

Two types of boundary conditions are used in this work. The *Dirichlet* boundary condition directly sets a value at the boundary, e.g. the function f takes on a fixed value c

$$f = c. \tag{3.22}$$

The *Neumann* boundary condition on the other hand fixes the value of the normal derivative at the boundary

$$\boldsymbol{\nabla} f \cdot \boldsymbol{n} = c, \tag{3.23}$$

where $\boldsymbol{n}$ is the unit vector normal to the boundary. In 1D this reduces to $\frac{\partial f}{\partial x} = c$.

The implementation of boundary conditions into a numerical scheme involves defining the value of each variable at the boundary. In the code used in this work, this has to be done at each step of the right-hand side calculation. Generally periodic boundary conditions are

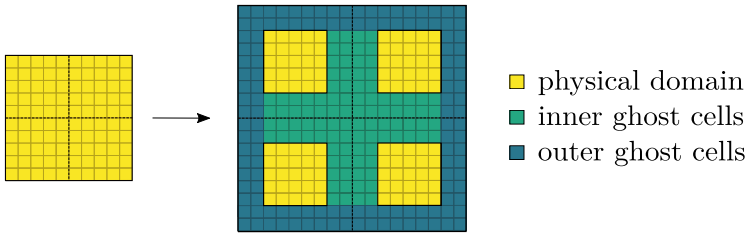

Figure 3.3: Schematic figure of the computational domain in two dimensions: It consists of the physical domain and the ghost cells. The code runs in parallel on multiple processors, among which the computational domain is divided into equal parts. The inner ghost cells are responsible for the communication between neighboring processors, while the outer ghost cells determine the boundary conditions.

used, which can be imagined as placing a copy of the physical domain at each boundary. However, special boundary conditions are required for the simulation of the magnetic reconnection model. Therefore the possibility to use different types of boundary conditions was implemented as part of this work.

3.3.1 Implementation

The boundary conditions are implemented using additional cells, so-called *outer ghost cells*. The total computational domain consists of the physical domain and the ghost cells. The code runs in parallel on multiple processors for an efficient computation using a *message-passing interface* (MPI) [29]. The communication between the processors is done with *inner* ghost cells. Each processor has two layers of ghost cells in each direction, which is shown schematically in figure 3.3 in two dimensions. They are necessary for the various steps of the RHS computation since information of neighboring cells either in the physical domain of neighboring processors or given by the boundary conditions are required. The maximum number of neighboring cells is required for the CWENO polynomial reconstruction, where two cells to the left and right of each cell are needed. Therefore at any boundary (inner or outer) values have to be assigned to these two additional ghost cells at each step of the calculation.

For the inner ghost cells, this is straightforward: neighboring processors have to exchange the information of the cells located at their shared boundary. In the case of periodic boundaries, the same applies to the outer ghost cells, as no actual physical outer boundary exists. Instead one can imagine copies of the physical domain to be attached to the boundaries, as shown in figure 3.4. However in the non-periodic case these values depend on the desired behavior at the boundary. There are many possibilities, three of which were implemented in this work: a zero-gradient, an antisymmetric and a constant boundary. In the zero-gradient approach, the values in the ghost cells are chosen symmetrically, such that the gradient at the boundary vanishes. This is a Neumann boundary condition as it specifies that the derivative at the boundary is zero. The other two cases are Dirichlet conditions: In the constant case, the outer ghost cells are set to a constant value c. In the antisymmetric case, the values in the outer ghost cells are obtained by point reflection at the boundary around the value c. The different types of non-periodic boundaries are shown in figure 3.4 in one dimension for $c = 0$.

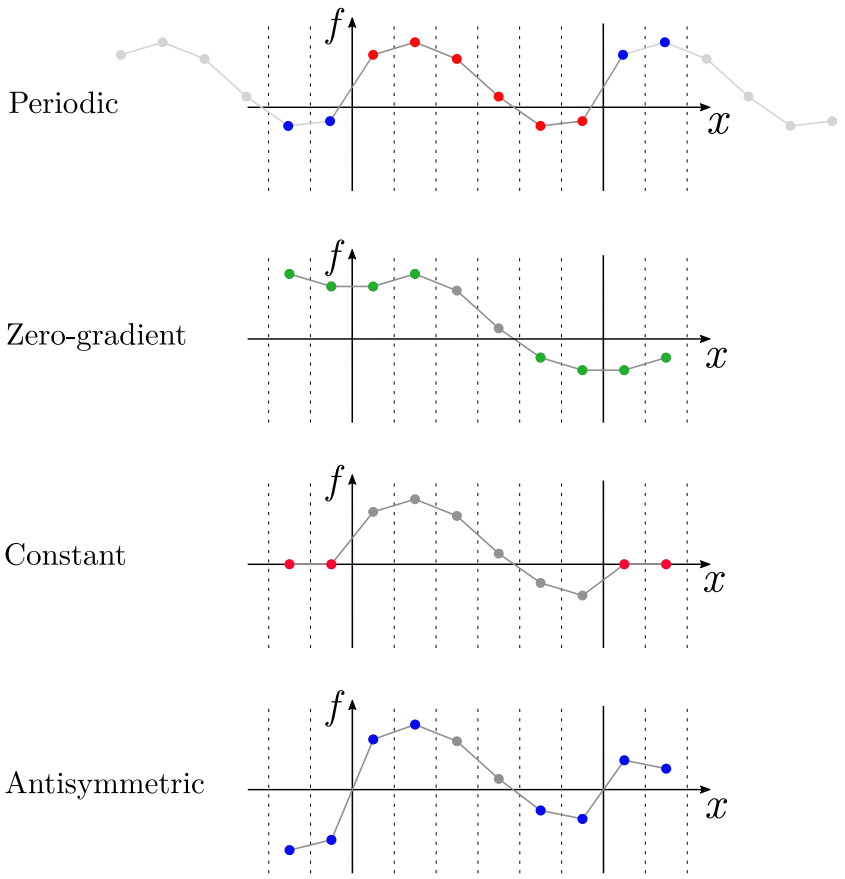

Figure 3.4: Implementation of boundary conditions shown in one dimension for some variable f: two additional cells, the outer ghost cells, are used to determine the behavior at the boundary. Periodic boundary conditions are achieved by placing copies of the physical domain at both sides. Three types of non-periodic boundary conditions are shown. In the zero-gradient one, the values in the ghost cells are found by reflection at the boundary. In the constant case, a constant value c is assigned to the ghost cells. Antisymmetric boundaries are achieved by a point reflection around a point c at the boundary. This is shown here for $c = 0$.

This procedure has to be adapted for each step of the right-hand side computation, depending on whether the variables are defined as cell-, face- or edge-averaged quantities. Furthermore, special care has to be taken when setting the boundary conditions for the magnetic field components to ensure that the solenoidality is maintained.

3.3.2 Application to the reconnection model

These boundary conditions can now be applied to the reconnection model. Periodic boundaries in the x and y-directions ensure the periodicity of the system. In the z-direction a combination of the above introduced possible types of boundary conditions has to be chosen for the various variables, as shown in table 3.1. As discussed in section 2.1.3, the magnetic field lines can be kept in place at the z-boundaries by using the so-called no-slip condition,

Table 3.1: Boundary conditions for the reconnection model: three different types of non-periodic boundary conditions were implemented, namely zero-gradient (zg), antisymmetric (as) and constant (c). Each variable is assigned a type of boundary condition to fulfill the requirements of the numerical reconnection model.

variable	ρ	$\boldsymbol{v}$	$\boldsymbol{B}$	$\boldsymbol{E}$
boundary condition	zg	as / c	zg	as / c

which means setting the velocity to zero. This can be done with the constant or antisymmetric boundary condition introduced above. For the remaining variables the boundary conditions are chosen in the following way:

The density ρ and the magnetic field components are set to zero-gradient boundaries. Although the electric field is not an independent variable, it has to be assigned a boundary condition as well for technical reasons. These have to be consistent with the boundary conditions chosen for $\boldsymbol{v}$ and $\boldsymbol{B}$. As $\boldsymbol{E} = -\boldsymbol{v} \times \boldsymbol{B}$, the boundary condition for the electric field has to be the same as for the velocity, i.e. constant or antisymmetric.

3.3.3 Convergence test

Both the finite-volume scheme and the time integration are fourth-order accurate. A convergence test was carried out to check whether the boundary conditions were implemented correctly and are suitable for the numerical experiments. The initial conditions of this one-dimensional test (in the y-direction) were chosen as follows:

$$\begin{pmatrix} \rho \\ \rho v_x \\ \rho v_y \\ \rho v_z \end{pmatrix}_{t=0} = \begin{pmatrix} 1 \\ A \exp(-\frac{1}{2\sigma^2}(y-\mu)^2) \\ 0 \\ 0 \end{pmatrix}, \qquad \begin{pmatrix} B_x \\ B_y \\ B_z \end{pmatrix}_{t=0} = \begin{pmatrix} 0 \\ 1 \\ 0 \end{pmatrix}. \tag{3.24}$$

The Gaussian function in the x-component of the momentum has a certain amplitude, A, standard deviation, σ and mean value, μ, which were chosen to be $A = 0.01$, $\sigma = 0.05$ and $\mu = 0.4$ for a computational domain of size $L_y = 1$.

The perturbation in the plasma momentum induces a deformation of the magnetic field line that creates a transversal Alfvénic pulse that propagates along the magnetic field line in both directions. Its speed is given by the Alfvén speed $v_A = \sqrt{\frac{B_0^2}{\mu_0 \rho_0}}$ associated with the mean field $B_y = 1$. After $t = 2\,t_A$ the wave has interacted with both boundaries and has returned to its initial position.

The convergence is tested by performing simulations for different resolutions N_y and using the highest resolution as a reference solution. An average error $\mathrm{d}U_{mean}$ is then computed by summing over the differences of all seven variables U_i at time $t = 2\,t_A$:

$$\mathrm{d}U_{mean}(N_y) = \frac{1}{7N_y} \sum_{i=1}^{7} \Big| U_i(N_y) - U_i(N_{y,max}) \Big|. \tag{3.25}$$

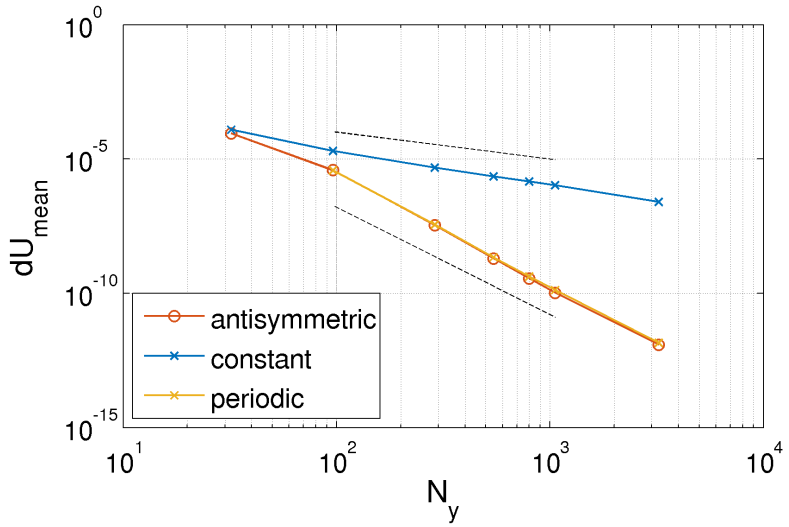

Figure 3.5: Convergence test for different types of boundary conditions: The convergence order is given by the slope (in a double-logarithmic plot) with which the mean error $\mathrm{d}U_{mean}(N_y)$ decreases when the resolution N_y is increased. Both the antisymmetric and periodic cases have a convergence order of four, while the constant case exhibits a convergence order of one, which is indicated by the dashed lines with the slopes -1 and -4.

The error was computed with the non-periodic boundaries listed in table 3.1 as well as periodic boundaries as a reference. The convergence order can be seen in the double logarithmic plot in figure 3.5. When the velocity boundary condition is constant, the error converges with order one, while in the antisymmetric and periodic cases the convergence order is four. The worse performance in the constant case could be due to unexpected cancellation effects in the polynomial reconstruction mechanism. Since the proper order of convergence is observed for the antisymmetric case, the simulations of the reconnection model are carried out with antisymmetric boundary conditions for the velocity and the electric field and zero-gradient boundaries for the density and the magnetic field.

3.4 Forcing

An external forcing is applied to the initially uniform system at rest to cause an entanglement of the magnetic field lines. In the numerical framework this is done by adding the force field $\rho\boldsymbol{F}$ multiplied by the time step Δt to the momentum term $\rho\boldsymbol{v}$ to give an updated momentum, in which the forcing is included:

$$(\rho\boldsymbol{v})_{new} = \rho\boldsymbol{v} + \rho\boldsymbol{F}(\boldsymbol{U}(t), \boldsymbol{B}(t), t)\Delta t.$$

3.4.1 Driving force

The forcing for the numerical experiment described in section 2.2.1 is used to drive the magnetic field to high spatial complexity and cause an entanglement of field lines. As it is periodic in the x and y-direction and falls to zero at the z-boundaries, it suits the no-slip boundary

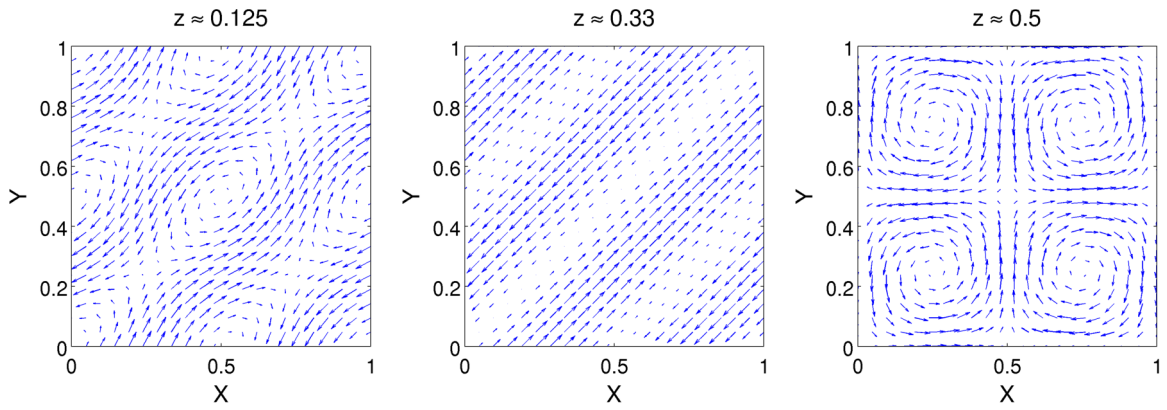

Figure 3.6: Force field $\boldsymbol{F}$ in the x-y plane at different z-positions (with $L = L_p = 1$): At $z \approx 0.125$ the field shows a slight twisting structure, which turns into a shearing structure at $z \approx 0.33$ and back to a more pronounced twisting in the middle of the domain. It should be noted that the amplitude of the vectors was rescaled such that the structure is easily discernible, but in fact the amplitude varies in the z-direction and falls to zero at the boundaries $z = 0$ and $z = 1$.

conditions. It is obtained by putting equations (2.39) - (2.42) together, giving the following expression:

$$\boldsymbol{F}(x,y,z,t) = F_0\,(1 - e^{-t/\tau}) \begin{pmatrix} f_x(x,y,z) \\ f_y(x,y,z) \\ f_z(x,y,z) \end{pmatrix}. \tag{3.26}$$

Here F_0 denotes the forcing amplitude. The components of the forcing are given by

$$\begin{aligned} f_x(x,y,z) &= \frac{2\pi}{L_p}\left(-\sin(\frac{2\pi x}{L_p})\cos(\frac{2\pi y}{L_p})\sin(\frac{\pi z}{L}) + \cos(\frac{2\pi x}{L_p})\sin(\frac{2\pi y}{L_p})\sin(\frac{2\pi z}{L})\right) \\ f_y(x,y,z) &= \frac{2\pi}{L_p}\left(\cos(\frac{2\pi x}{L_p})\sin(\frac{2\pi y}{L_p})\sin(\frac{\pi z}{L}) - \sin(\frac{2\pi x}{L_p})\cos(\frac{2\pi y}{L_p})\sin(\frac{2\pi z}{L})\right) \\ f_z(x,y,z) &= 0. \end{aligned} \tag{3.27}$$

It is constant in time up to a factor of $(1 - e^{-t/\tau})$. This is well suited for the problem as it does not introduce any probabilistic process into the system, which itself is expected to behave chaotically. Three z-slices of the force field are shown in figure 3.6.

3.4.2 Damping layers

Additionally, damping layers are included close to the z-boundaries to damp perturbations caused by Alfvén waves propagating along the magnetic field lines. They further ensure that the velocity remains zero at the z-boundaries, so that the footpoints of the field lines remain fixed. They have a certain thickness, r_{damp}, which if not stated otherwise is set to 10% of the computational domain. The force field described above is then applied to the remaining inner part of size $L_F = L - 2r_{damp}$ by replacing the argument of the sinusoidal functions in z in

equation (3.27):

$$\frac{z}{L} \rightarrow \begin{cases} \frac{(z-r_{damp})}{L_F} & \text{if } r_{damp} \leq z \leq (L - r_{damp}) \\ 0 & \text{otherwise} \end{cases}. \tag{3.28}$$

The damping is achieved by introducing a friction term in the momentum equation corresponding to

$$\partial_t v = -\frac{v}{\tau_d}. \tag{3.29}$$

The solution to this equation is an exponential decay $v \propto e^{-t/\tau_d}$ with a time constant τ_d. In practice, the damping is included by updating the momentum with the additional friction term multiplied with the time step Δt in the damping layers:

$$(\rho \boldsymbol{v})_{new} = \rho \boldsymbol{v}(1 - \frac{\Delta t}{\tau_d}). \tag{3.30}$$

It can be easily seen from equation (3.30) that the damping strength increases with decreasing τ_d. However, τ_d should be much larger than the time step Δt, as otherwise the exponential decay becomes very steep. This would make the equations stiff, which would then require an unnecessary small time step in order to prevent the numerical method from becoming unstable.

4 Simulations and Post-processing

The code described in the previous section is used to perform simulations of the numerical model introduced in section 2.2.1. This chapter provides an overview of the different simulation runs and their parameters and explains how the data is further processed. Various diagnostic quantities are computed by the post-processing program, which was implemented in Fortan90 as part of this work and is based on the diagnostic tools presented in [17].

4.1 Simulation runs

Several simulation runs were carried out with varying parameters, which are summarized in table 4.1. They were run on the cluster of the math department of the Technical University Berlin and on the high performance-computing (HPC) system Draco of the Max Planck Computing and Data Facility (MPCDF).

In the first set of simulations A1-A3 the damping constant is varied in order to investigate the effect the damping layers have on the system. The second set of runs B1-B5 and the third set C1-C5 are used to study the dependence on the grid resolution and the forcing amplitude, respectively.

Table 4.1: Parameters of the simulation runs evaluated in this work

Run	Resolution N	Forcing amplitude F_0	Damping constant τ_D
A1	64	0.2	-
A2	64	0.2	0.1
A3	64	0.2	0.05
B1	48	0.2	0.05
B2	64	0.2	0.05
B3	96	0.2	0.05
B4	128	0.2	0.05
B5	256	0.2	0.05
C1	64	0.10	0.05
C2	64	0.15	0.05
C3	64	0.20	0.05
C4	64	0.30	0.05
C5	64	0.40	0.05

The initial conditions were set to

$$\begin{pmatrix} \rho \\ \rho v_x \\ \rho v_y \\ \rho v_z \end{pmatrix}_{t=0} = \begin{pmatrix} 1 \\ 0 \\ 0 \\ 0 \end{pmatrix}, \qquad \begin{pmatrix} B_x \\ B_y \\ B_z \end{pmatrix}_{t=0} = \begin{pmatrix} 0 \\ 0 \\ 1 \end{pmatrix} \tag{4.1}$$

for all runs. The computational domain was chosen to be cube-shaped with a side length of $L = L_p = 1$. With these parameters the Alfvén speed and Alfvén transit time (the time an Alfvén wave needs to travel across from bottom to top plate) become $c_A = 1$ and $t_A = 1$. The isothermal sound speed is set to $c_s = 1$. The time constant that regulates the forcing amplitude (equation (3.26)) is set to $\tau = 0$, such that the forcing is constant in time.

4.2 Post-processing

The simulations produce time frames of the density, the momentum and the magnetic field. The time evolution of these variables or related quantities, such as the magnetic energy, can give insight into the dynamics of the system. In order to investigate potential reconnection events in detail, however, the magnetic field line coordinates are required. They are obtained by running a post-processing program over each frame returned from the simulations. The main steps of the program are shown in the flowchart in figure 4.1 and can be summarized as follows:

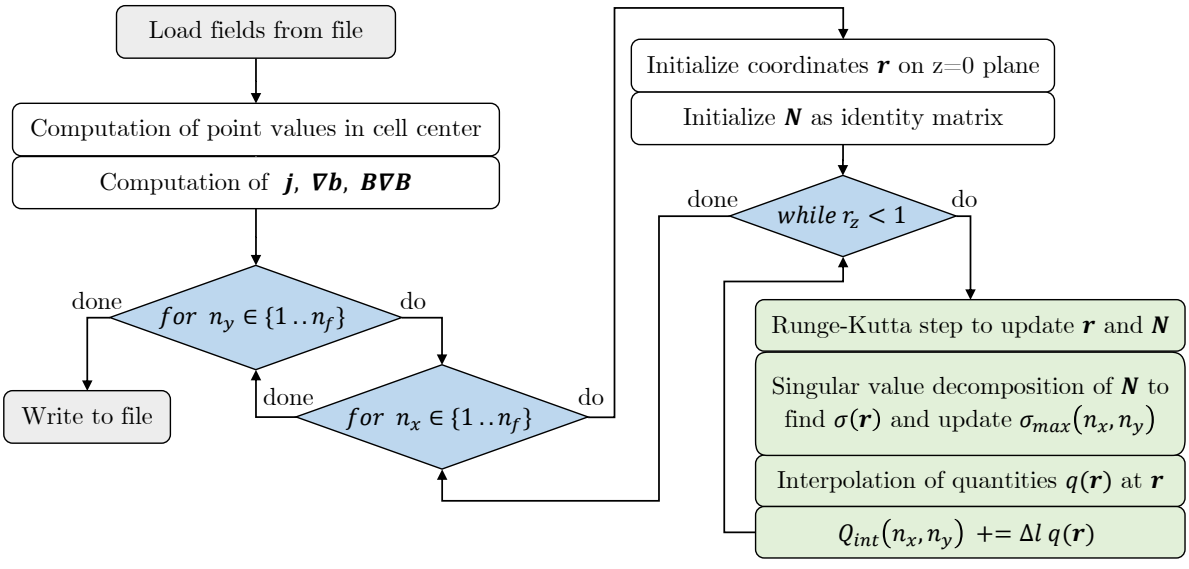

Figure 4.1: Flowchart visualizing the main steps in the post-processing: the fields from the simulation are used to find the coordinates $\boldsymbol{r}$ of $n_f \times n_f$ magnetic field lines and simultaneously compute the exponentiation number σ from the matrix $\boldsymbol{N}$ by solving equations (2.53) and (2.59), respectively. The quantities q (kinetic energy, parallel current density and the parallel magnetic tension) are integrated along the field lines by computing their value at position $\boldsymbol{r}$ and adding them to the integral Q_{int} for each field line.

The fields loaded from the time frame are given as cell- or face-averaged quantities for the hydrodynamic variables and the magnetic field components, respectively. In a first preparation step these are transformed into point values in the center of each cell, from which the current density, $\boldsymbol{j}$, the Jacobian matrix of the normalized magnetic field, $\boldsymbol{\nabla b}$, and the magnetic tension term, $\boldsymbol{B\nabla B}$, are computed.

The main part of the program consists of two loops over the y and x position of the field lines, which form an equally-spaced grid of $n_f \times n_f$ field lines. Each starting point is labeled by (n_x, n_y) with $n_x, n_y \in \{1..n_f\}$. The field line coordinates are initialized on the $z = 0$ plane and the matrix exponent $\boldsymbol{N}$ (see section 2.2.3) is initialized as a 3×3 identity matrix.

The coordinates of each magnetic field line are computed with a constant step size Δl, by solving equation (2.53) with a fourth-order Runge-Kutta method (RK4, see section 3.2) until the $z = 1$ plane is reached. Simultaneously, equation (2.59) is solved to find the matrix $\boldsymbol{N}$ at the position $\boldsymbol{r}$. In general the coordinates $\boldsymbol{r}$ will not coincide with the points in the cell centers, on which the quantities are defined. Therefore an interpolation method is necessary, so that e.g. the magnetic field can be computed at any position $\boldsymbol{b}(\boldsymbol{r})$, from which in turn the coordinate $\boldsymbol{r}$ is updated (equation (2.53)). In this program a tricubic interpolation method is used [21].

For each integration step a singular value decomposition (using the Linear Algebra Package (LAPACK) [2]) of matrix $\boldsymbol{N}$ is done, from which the exponentiation number $\sigma(\boldsymbol{r})$ is found as the logarithm of the largest singular value (see section 2.2.3). Finally, the kinetic energy, parallel current density and the parallel magnetic tension are integrated along the field lines, by computing their value q at position $\boldsymbol{r}$ through interpolation and then summing over these points to get the integrated value:

$$Q_{int} = \Delta l \cdot \sum_{r_z=0}^{r_z=1} q(\boldsymbol{r}).$$

In general only the footpoints of the field lines, the maximum exponentiation number σ_{max} and the integrated quantities along each field line are returned due to memory limitations. For a small selected number of field lines the coordinates and the profiles of the various quantities

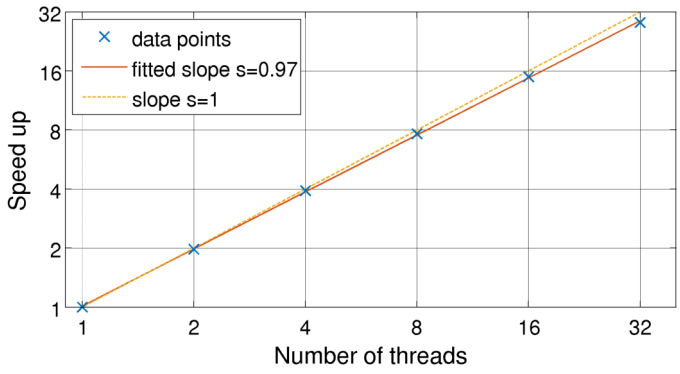

Figure 4.2: Efficiency of the parallelization: the speed up achieved is close to the ideal case, in which it scales with the number of threads. 300×300 field lines were integrated with a step size of $\Delta l = 0.01$ and grid resolution of 256^3.

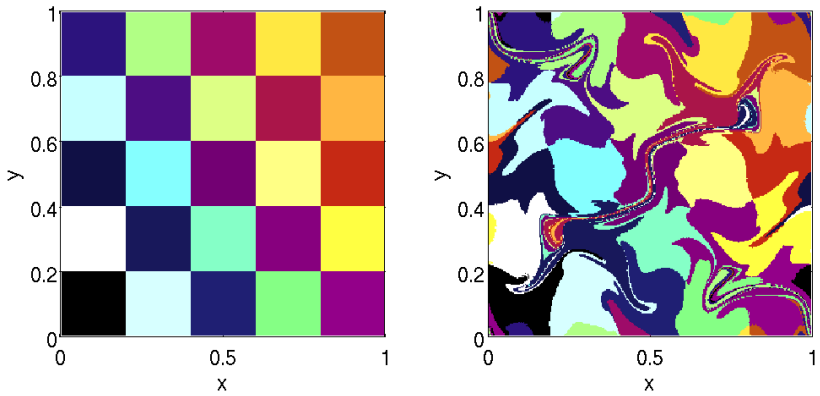

Figure 4.3: Coarse-grained mapping of the field line footpoints: The end points on the top plate are divided into a 5×5 grid, which is colored in a checkerboard pattern (left). They are then mapped onto the starting points on the bottom plate, such that changes in the mapping can be seen as a distortion of the pattern (right).

along them can be returned, when the behavior of the whole field line is of interest or for visualization purposes.

The outermost loop over the y-coordinates of the starting points was parallelized using the shared memory interface Openmp [12], which allows the distribution of tasks to multiple threads. This approach is well suited to the problem, as the individual field lines and thus the individual tasks are independent of each other. The speedup shown in figure 4.2 is almost equal to the number of threads used, which is limited to 32 due to the architecture of the computation nodes on the cluster used in the framework of this work. It is measured by timing the parallel section of the program, which is run on a 256^3 frame with the parameters $n_{fl} = 300$ and $\Delta l = 0.01$.

4.2.1 Footpoint diagnostics

The output of the post-processing can be used to gain further insight into the dynamics of the field lines. The mapping of footpoints from bottom to top is useful to identify potential reconnection events. This is visualized by applying a coarse-grained grid to the end points at the top plate and assigning colors in a checkerboard pattern. These are then mapped onto the equally-spaced starting points, as described in [17] and shown in figure 4.3 for a frame of simulation A3. The distortion of the checkerboard pattern highlights the regions in which reconnection might have occurred, as a reconnection event necessarily leads to change in the footpoint mapping. However, the reverse is not true; a change in the mapping does not mean that field lines reconnected. Instead, due to numerical resistivity, the field lines can diffuse through the plasma, as Alfvén's theorem only holds in the ideal MHD case. Therefore not only the mapping of footpoints but also the time scales on which changes in the mapping occur need to be considered in order to discriminate between field line diffusion and reconnection.

Subtracting the end points of two consecutive frames from each other gives rise to a footpoint drift. The drift of a single point, $p(t)$, divided by the time step between the two frames, $\Delta\tau$,

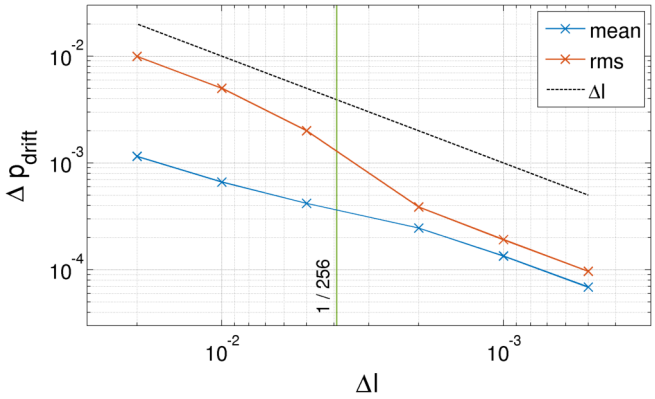

Figure 4.4: Convergence of footpoint drift for decreasing integration step size Δl: The scaling of the mean and the RMS of the footpoint drift error Δp_{drift} and the rough error estimate Δl are shown for a grid size of 256^3.

corresponds to a mean footpoint velocity

$$v_{fp}(t) = \frac{\left|p(t+\Delta\tau) - p(t)\right|}{\Delta\tau} = \frac{p_{drift}}{\Delta\tau}. \tag{4.2}$$

In the limit $\Delta\tau \to 0$ this evidently turns into the instantaneous velocity at time t.

Due to the periodic boundaries in the x and y-direction, the maximum distance two points can have at any time is given by $\sqrt{0.5}$, which in turn gives an upper bound for the footpoint velocity for a given time step $\Delta\tau$. For a low time resolution (that is a large $\Delta\tau$) the maximal possible velocity is comparatively low and easily saturated, giving a rough overview over the potential reconnection regions. Conversely, a small $\Delta\tau$ makes it possible to resolve single events with large footpoint velocities, but contains limited information about the system changes on large scales. Therefore, in order to capture reconnection events, different time intervals between frames need to be considered.

Estimation of the step size Δl

The accuracy of the computed footpoint velocity depends on the accuracy of the end points, which in turn is limited by the integration step size Δl. The error in the footpoint drift can therefore be roughly estimated as

$$\Delta p_{drift} \sim \Delta l.$$

In order to check this estimation a convergence test is carried out, in which the footpoint drift of each field line (with a time step of 0.001 t_A and a resolution of 256^3) is computed for varying step sizes. The footpoint drift of the smallest step size $\Delta l = 3 \times 10^{-4}$ serves as a reference solution. It is subtracted from the footpoint drift computed with the different step sizes for each field line. The mean value of the error is then obtained by averaging over the absolute value of the error of all field lines. Another measure is given by the root-mean-squared error (RMSE), which is the square root of the averaged squared error. It differs from the mean value, in that it gives more weight to larger errors and is thus more sensitive to outliers. Both measures are plotted against the step size with logarithmic scales in figure 4.4. It can be seen

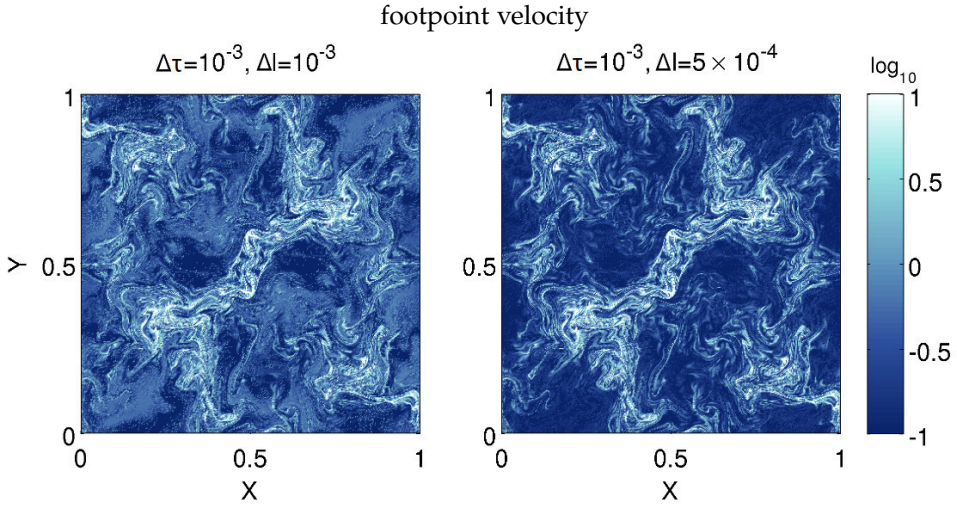

Figure 4.5: Footpoint velocity computed from two consecutive frames (of run B5) with a time step of $\Delta\tau = 10^{-3}$ and an integration step size of $\Delta l = 10^{-3}$ (left) and $\Delta l = 5 \times 10^{-4}$ (right).

that both are smaller than the estimate for all step sizes. While the mean error is about an order of magnitude smaller, the RMSE is initially closer to the estimated value. However for step sizes smaller than the grid size of $1/256$, both measures are of the same order of magnitude and scale with Δl as expected. This shows that using Δl as an upper bound for the error is a reasonable choice.

As stated above, the maximum distance between two end points is given by $\sqrt{0.5} \approx 0.7$. An integration step of $\Delta l \lesssim 10^{-3}$ is necessary in order to resolve drifts of the order of 10^{-2}. Additionally the time step $\Delta\tau$ should be taken into consideration when choosing the integration step size Δl, as the error in the footpoint velocity can be roughly estimated as

$$\Delta v_{fp} \sim \Delta l / \Delta\tau.$$

Therefore at higher time resolutions, the spatial integration step size should be decreased, in order to resolve roughly the same range of footpoint velocity. However, the computation time scales with the integration step size and the number of field lines, such that a compromise has to be found: For simulations with time steps $\Delta\tau \geq 10^{-2}$ the step size $\Delta l = 10^{-3}$ was used. The smallest time step used is $\Delta\tau = 10^{-3}$, for which a step size of $\Delta l = 5 \times 10^{-4}$ was chosen. The difference in resolution can be seen in figure 4.5, in which the footpoint velocity of 400×400 field lines is shown for both integration step sizes with the smallest time step. While the overall structure is similar in both cases, the one with the larger step size shows a higher noise level, such that some details of the fine-structure are not resolved well.

Footpoint velocity distribution

Finally, the distribution of the footpoint velocity and its evolution in time can be studied and a criterion for distinguishing between the comparatively slow and gradual diffusion of field lines and the quick and spontaneous reconnection process can be derived.

The footpoint velocity follows a log-normal distribution, the probability density function (pdf) of which can be derived from the pdf of a normal distribution $f(x)$ by considering the integral

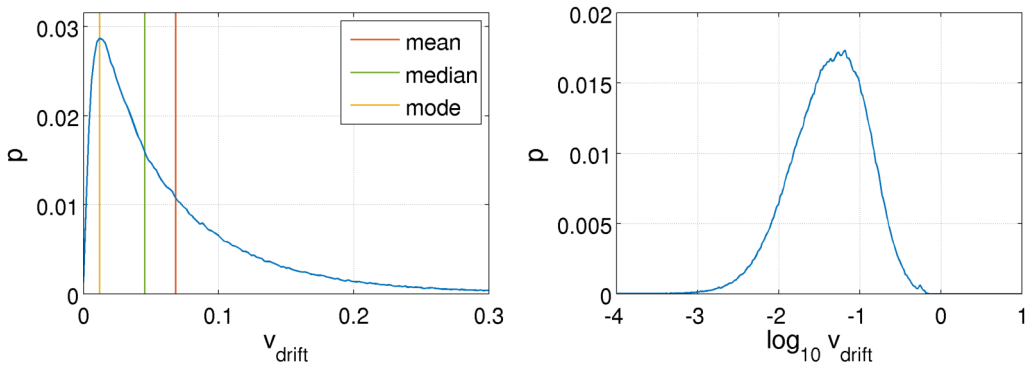

Figure 4.6: footpoint velocity distribution: The data is distributed according to a log-normal distribution (left). The mean, median and mode are measures that characterize the central tendency and can be used to define a reconnection threshold. After taking the logarithm, the data follows a normal distribution (right).

over the whole domain

$$\int_{-\infty}^{\infty} f(x)\,\mathrm{d}x = 1$$

and substituting $x = \ln y$, such that $\mathrm{d}x = \mathrm{d}y/y$, giving

$$\int_{-\infty}^{\infty} \frac{1}{\sqrt{2\pi\sigma^2}} \exp\left(-\frac{(x-\mu)^2}{2\sigma^2}\right) \mathrm{d}x = 1$$
$$\int_{0}^{\infty} \frac{1}{\sqrt{2\pi\sigma^2}} \frac{1}{y} \exp\left(-\frac{(\ln y-\mu)^2}{2\sigma^2}\right) \mathrm{d}y = 1.$$

Here μ and σ denote the mean and standard deviation of the normal distributed variable x. The pdf of the log-normal distribution is then given by

$$f(y) = \frac{1}{\sqrt{2\pi\sigma^2}} \frac{1}{y} \exp\left(-\frac{(\ln y-\mu)^2}{2\sigma^2}\right).$$

By taking the logarithm of a log-normal distributed variable X, a normal distributed variable $Y = \ln X$ is obtained [30]. This is true regardless of the chosen base. In the following a logarithm with base 10 is used, as this captures the several orders of magnitude over which the footpoint velocity is distributed. The pdf's of both the footpoint velocities and their logarithm are shown in figure 4.6 (computed for a few frames of run C at a time step $\Delta\tau = 1$).

In order to distinguish between a fast (reconnection) event and slower processes, a threshold for the footpoint velocity can be set. There are three different measures which can be used to describe the central tendency of the distribution: the mean, the median and the mode, all of which are shown in figure 4.6 for the log-normal distribution. While the mode of the distribution corresponds to the most common value and is thus located at the peak, the mean is shifted to higher values due to the distribution's long tail. The median marks the point at which half of the values are distributed below and above it [30]. Which measure is best suited is further discussed based on the results in the following chapter.

Furthermore, these measures multiplied with the time step $\Delta\tau$ give an estimate for the typical length scale on which the events occur. This can be used to determine the radius of field line bundles, which can be traced in order to visualize individual events.

4.2.2 Correlation

Running the post-processing program over several time frames results in time series of quantities such as the exponentiation number and the footpoint velocity for each field line. The theory states that field lines with a high exponentiation number, σ_{max}, are especially sensitive to non-ideal effects. Therefore, it is expected that the footpoint velocity along these field lines is large as well. Any occurrences of enhanced footpoint velocity (peaks in the time series) are of interest, as they are potential reconnection events. They can be compared to the exponentiation number by considering the temporal correlation of these two quantities.

One way of evaluating the linear correlation of two variables X and Y is using Pearson's correlation coefficient ρ_{XY}. It is defined as

$$\rho_{XY} = \frac{\mathrm{cov}(X,Y)}{\sigma_X \sigma_Y}, \tag{4.3}$$

with the covariance $\mathrm{cov}(X,Y)$ given by

$$\mathrm{cov}(X,Y) = \frac{1}{T-1} \sum_{i=1}^{T} \left(X_i - \mu_X\right)\left(Y_i - \mu_Y\right). \tag{4.4}$$

Here μ_X, μ_Y, σ_X and σ_Y denote the mean values and the standard deviations of variables X and Y, and T is the number of frames in the time series. The correlation coefficient ranges from -1 to 1, where -1 corresponds to a negative and +1 to a positive linear correlation. When it is zero the variables show no linear correlation [11].

Furthermore, the duration of an event can be estimated from the autocorrelation function of the time series of the footpoint velocity. The autocorrelation function $r(\tau)$ of a time series of variable X measures the correlation between X_t and $X_{t+\tau}$:

$$r(\tau) = \frac{\mathrm{cov}(X_t, X_{t+\tau})}{\mathrm{var}(X)}, \tag{4.5}$$

where τ is the lag by which the function is shifted and the sum in the covariance in equation (4.4) goes from $i = 1$ to $i = T - \tau$. As before, the function can take on values between -1 and 1 and is defined such that it is maximal at $\tau = 0$ [11].

Now the event duration τ_{event} can be obtained by finding the lag at which the autocorrelation falls below a certain threshold, for example $1/e$. This essentially is a measure of the broadness of the event peak.

5 Results

In this chapter the data produced by the simulations is analyzed with the diagnostic tools described in the previous chapter. The mean magnetic and kinetic energy give a general overview of the system's evolution, which can be divided into different phases. Furthermore the diagnostic quantities along the integrated magnetic field lines offer more insight into the field line behavior. As discussed in the previous chapter, the exponentiation number measures the degree of entanglement and the footpoint velocity is used to identify potential reconnection events. The integrated parallel electric field V (equation (2.28)) is a measure of non-ideal effects, but as in this work the resistivity is of numerical origin and of unknown magnitude the integrated parallel current density is used instead. Additionally, the kinetic

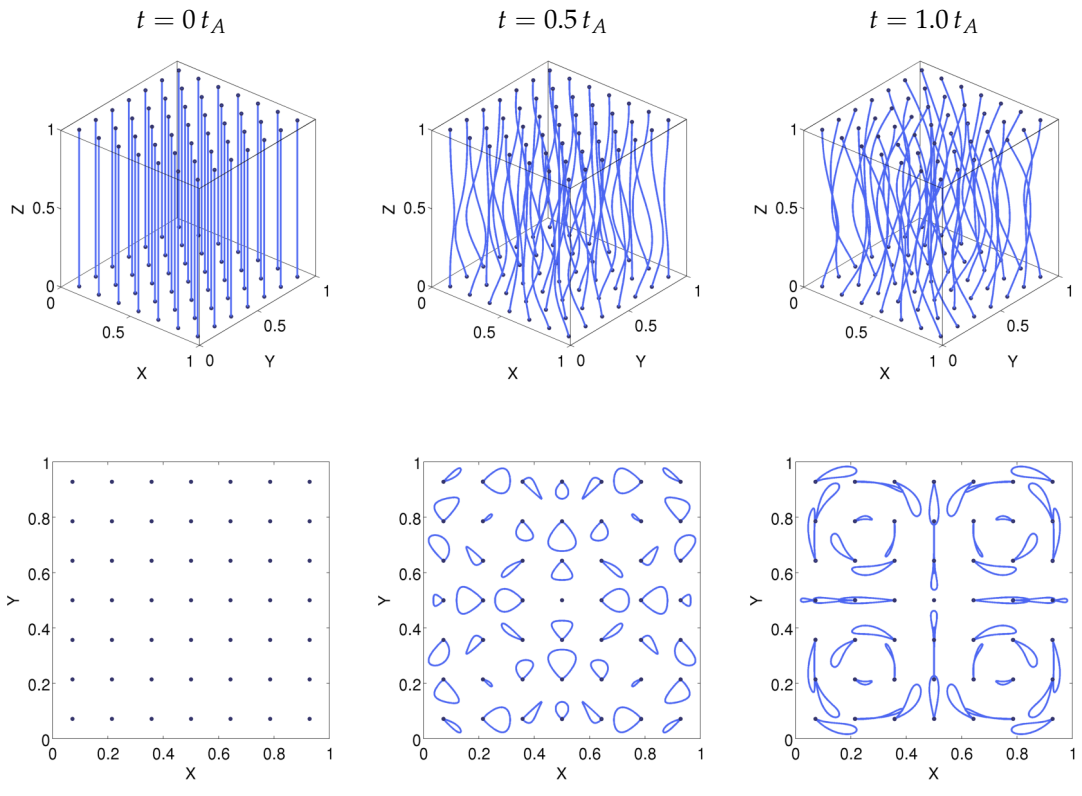

Figure 5.1: Snapshots of magnetic field lines reacting to the external forcing for simulation A3: (a) side view of the computational domain and (b) top view of the x-y plane. The field lines are distorted by the forcing while maintaining their footpoint positions.

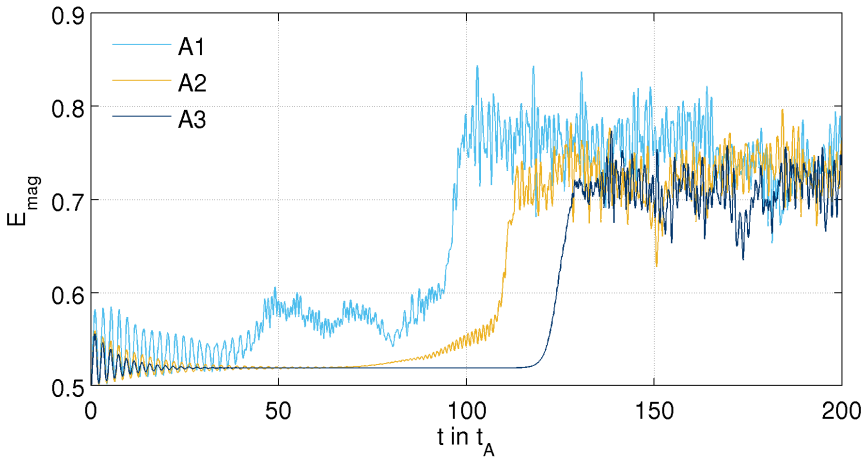

Figure 5.2: Time evolution of the magnetic energy for varying damping strengths (A1: no damping, A2: $\tau_d = 0.1$, A3: $\tau_d = 0.05$). While in all cases there are initial oscillations and a sharp increase in energy at some time, the behavior between these events differs. The fluctuations before the rise of magnetic energy present in run A1 are increasingly damped in runs A2 and A3.

energy and the parallel magnetic tension are integrated along the field lines, as magnetic reconnection is associated with a conversion of magnetic to kinetic energy and presumably changes the curvature of the field lines. Using these diagnostics on the three different sets of simulation runs listed in table 4.1, the system's evolution is studied in further detail with respect to the damping layers (set A), the resolution (set B) and the forcing amplitude (set C). Finally, a statistical analysis of the high resolution run B5 is presented, in which the correlation of the exponentiation number and the footpoint velocity is investigated.

5.1 Overview of the system evolution

The general behavior of the magnetic field is shown for simulation A3. The initially uniform magnetic field is distorted by the forcing, as can be seen in figure 5.1, where the magnetic field lines are shown at three different time steps. The footpoints of the field lines remain fixed at their initial positions, such that in the top view of the x-y plane the field lines form closed loops. This shows that the boundary conditions work in the desired way.

In order to investigate not only the dynamics of a few field lines but of the whole system, the time evolution of the magnetic energy is studied. It is shown in figure 5.2 for simulations A1-A3, in which the damping constant τ_d is varied. As the magnetic field strength initially is $B_0 = 1$, the magnetic energy starts at $E_{mag} = 0.5$. The total energy is not conserved, because of the applied kinetic forcing.

The behavior is similar for all three runs: in the beginning the energy oscillates as the abrupt switch-on of the forcing triggers Alfvén waves that travel along the magnetic field lines. At some point there is a sharp increase in energy followed by fluctuations around some higher energy level. Without damping (A1) the energy already fluctuates from the beginning, while in the presence of the damping layers (A2, A3), which continuously decrease the propagating

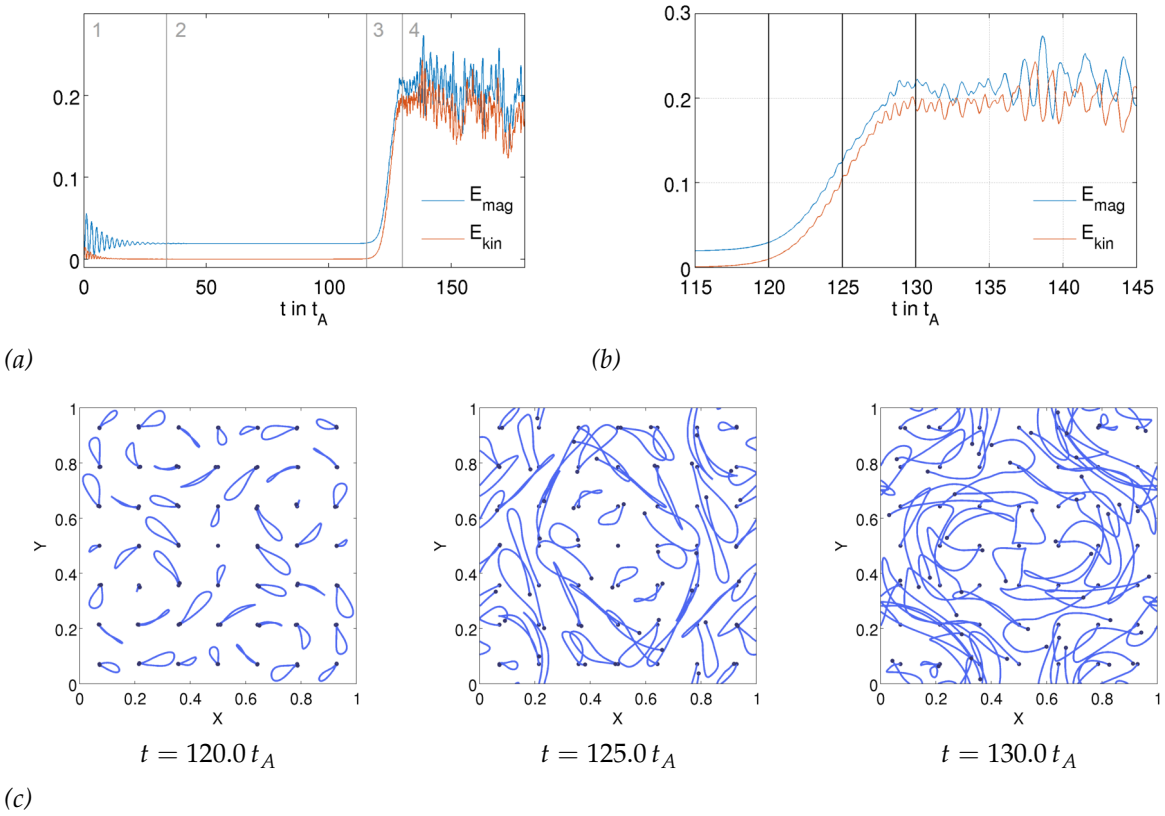

Figure 5.3: Time evolution of the magnetic and kinetic energy for run A3: (a) both the kinetic and magnetic energy initially oscillate (1) until they relax to a stationary state (2), followed by a transition (3) to a higher fluctuating energy level (4). A zoom-in of the onset and chaotic phase is shown in (b), where the vertical lines mark the times for which snapshots of the magnetic field line configurations are shown before, during and after the transition (c). Note that the initial magnetic energy of 0.5 was subtracted from the total magnetic energy in the (a) and (b).

Alfvénic fluctuations, it instead relaxes to a nearly stationary state, which persists longer the stronger the damping. As the main interest lies in the increase in energy and the strongly fluctuating behavior following it, the damping constant $\tau_d = 0.05$ of run A3 is used in all subsequent runs.

The system's evolution is investigated further for the damped run A3. Not only the magnetic energy, but also the kinetic energy is of interest. Both are shown in figure 5.3a for run A3, where the initial magnetic energy was subtracted, and it can be seen that their evolution is similar. It can be roughly divided into four phases: the relaxation phase, the stationary phase, the onset phase and the chaotic phase.

During the relaxation phase both the magnetic and kinetic energy oscillate before reaching a constant level, which in case of the kinetic energy is zero. This means that the system relaxes into a flow-free state, as the external forcing is balanced by the remaining forces. The field lines settle into a twisted state (see field lines at $t = 120\,t_A$ in figure 5.3c) in the stationary phase, corresponding to an increased constant magnetic energy. The possibility of this force balance is discussed in section IV of [10] and can be qualitatively understood by considering

that the Lorentz force acts as a restoring force to straighten the magnetic field lines that have been deformed by the forcing. The initial damped oscillations can then be interpreted as the interplay of the $\boldsymbol{j} \times \boldsymbol{B}$ force with the external force. The damping layers enable the force balance to occur in the first place, as they lead to the damping of perturbations caused by Alfvén waves traveling along the field lines, that would otherwise disturb the system. This is supported by the fact that in the undamped case in figure 5.2 no stationary state is reached.

The onset phase occurs once the force balance is disrupted and the forcing puts energy into the system again. The suddenness and steepness at which the increase in energy occurs suggests that this is caused by a reconnection process. The field lines in the stationary phase are in an entangled state and due to the increased sensitivity to resistive effects this can trigger reconnection. This disrupts the force balance as magnetic energy is converted into kinetic energy, which in turn increases the entanglement of field lines thereby triggering more reconnection processes.

In the chaotic phase the system fluctuates strongly around an increased energy level, as shown in 5.3b. Here the magnetic and kinetic energy show an approximately inverse relation characteristic of Alfvénic fluctuations: the kinetic energy increases, when the magnetic energy decreases and vice versa, which shows that an exchange of energy is occurring, overlayed with fluctuations of the total energy caused by the forcing. While it is possible that further reconnection processes happen in the chaotic phase, another interpretation is that the reconnected field configuration allows for additional freedom for the excitation of Alfvénic fluctuations by the forcing. This state would thus be a bath of propagating Alfven wave packets.

Furthermore, changes in the field line configuration can be observed during the onset. The field lines are shown before $(t = 120\, t_A)$, during $(t = 125\, t_A)$ and after $(t = 130\, t_A)$ the onset in figure 5.3c and it can be seen that they become increasingly chaotic. While in the first frame the footpoints at the bottom and top plate still coincide, the mapping changes in the second and even more so in the third frame, such that in the x-y projection the field lines no longer form closed loops. This means that non-ideal effects either cause the field lines to diffuse across the plasma or to reconnect with each other.

5.2 Stationary and onset phases

Before going into more detail regarding the changes in the footpoint mapping, the stationary state and the nature of the onset are further investigated. This is done by studying how the kinetic energy evolution is affected by the resolution and forcing strength.

5.2.1 Resolution dependency

The evolution of the kinetic energy is shown for different resolutions N in figure 5.4a with a logarithmic scale. While the overall behavior is similar in all cases, they differ with respect to the duration of the initial oscillations, the energy level of the stationary phase $E_{kin,eq}$ and the point in time at which the energy increases t_{onset}.

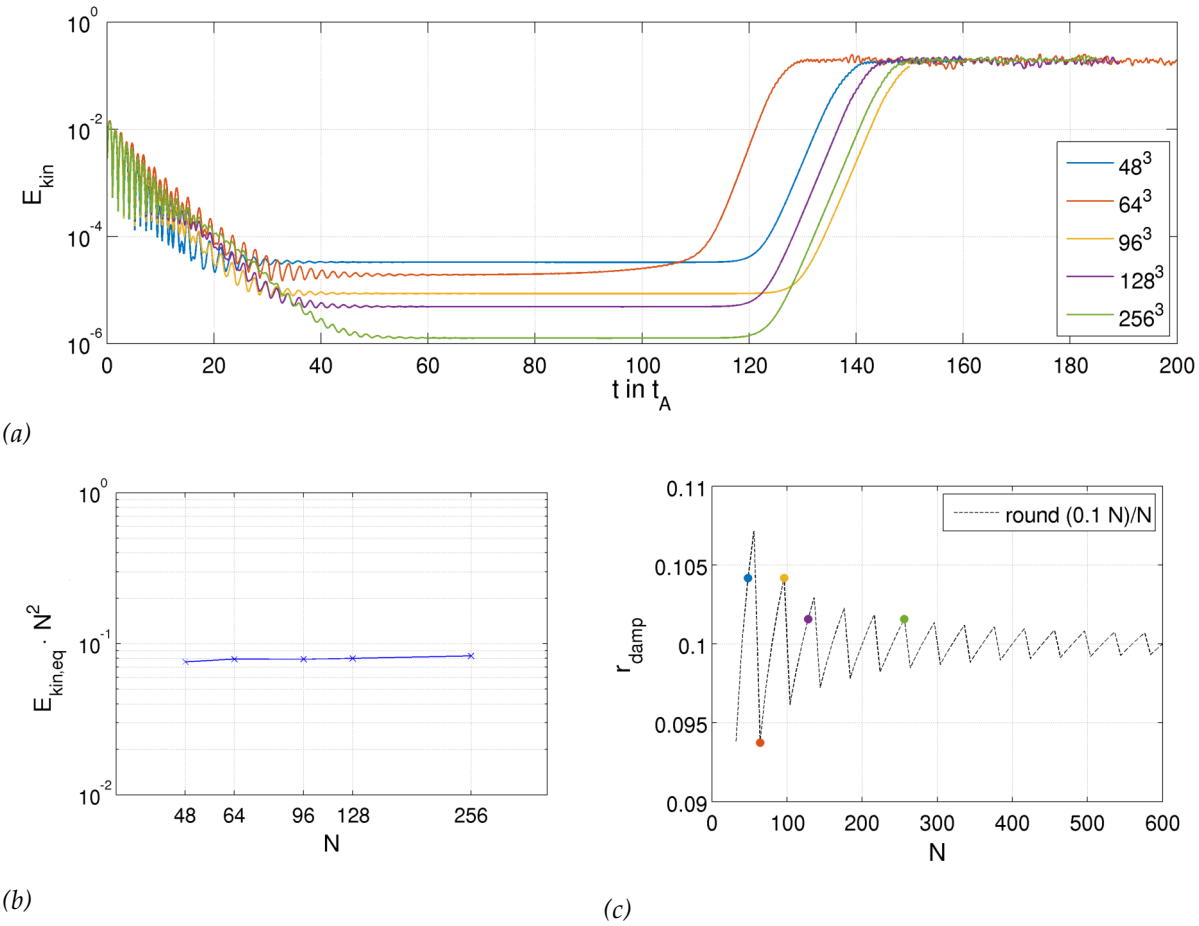

Figure 5.4: Kinetic energy evolution for different resolutions (runs B1-B5) (a): The equilibrium energy $E_{kin,eq}$ reached during the stationary phase scales as $\sim N^{-2}$ (b). The onset time does not increase regularly with the resolution, which is due to the fact that the resolution also influences the actual thickness of the damping layers, which affects the onset time (c).

The equilibrium kinetic energy is approximately zero. It can be observed that it scales with the resolution as $E_{kin,eq} \sim 1/N^2$, as shown in figure 5.4b, where the energy compensated with N^2 is approximately constant. This scaling can be understood by considering that the energy is computed from cell averaged quantities, such that it is second order accurate and the error scales with $\sim \Delta x^2 = N^{-2}$. This is reflected in the scaling of the energy level, which essentially corresponds to the numerical background noise.

When the resolution and thus the accuracy of the numerical scheme is increased, the numerical diffusion is expected to decrease, which in turn is expected to delay the onset time. The obtained results, however, show no monotone relation between the resolution and the onset time, e.g. the onset for a resolution of 96^3 occurs later than for the highest resolution of 256^3. An explanation for this seemingly random behavior is that among the numerical diffusion other parameters are affected by a change of resolution. In particular, the damping layers were set to a thickness of 0.1 for all cases, which translates to a certain amount of cells , i.e. $0.1\,N$ rounded to an integer value. Now depending on the resolution the actual thickness of

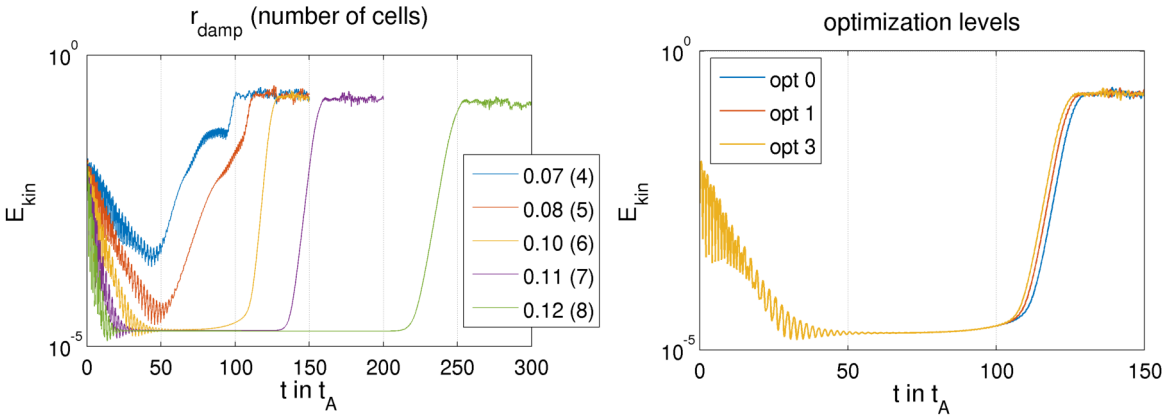

Figure 5.5: Sensitivity of the kinetic energy evolution at a resolution of 64^3: (left) the thickness of the damping layers r_{damp} influences the onset time significantly, where an increase in r_{damp} shifts the time to higher values. (right) Changing the optimization level when compiling also leads to a slight shift in the time, illustrating that the system is highly sensitive to even a slight change.

the damping layers

$$r_{damp} = \text{round}(0.1\,N)/N$$

is then slightly above or below the preset value of 0.1, as shown in figure 5.4c. The colored dots highlight the resolutions which were investigated, and it appears that this slight difference in size of the damping layers can contribute to explaining the observed onset times. For example, comparing the resolutions 48^3 and 64^3, it can be seen that the thickness of the damping layers in these two cases is at its highest and lowest value, respectively. This is reflected in the fact that the onset occurs earlier for the higher resolution of 64^3. The same is true at a resolution of 96^3, which has comparatively thick layers and for which the onset occurs the latest. This agrees with the behavior shown in figure 5.2, where an increase in the strength of the damping causes a delay in the onset time.

In order to check if the differences in r_{damp} can indeed explain the irregular shifts in the onset times at different resolutions, simulations at resolution 64^3 with different r_{damp} were carried out. The results are shown in figure 5.5. As the number of damped cells increases from four to eight, the stationary state is reached quicker as perturbations are damped more effectively. Furthermore the onset time is shifted regularly to higher values, showing that a slight change in the damping layer thickness has a significant effect on the behavior. This suggests that the size of the damping layers influences the stability of the stationary phase or in turn that perturbations that were not completely damped could trigger the reconnection process.

The sensitivity of the onset time is not restricted to the damping layers. For example, changing the optimization level of the compiler also affects the time evolution shown on the right in figure 5.5. While initially the difference between the three curves is of the order of the numerical accuracy $\sim 10^{-16}$ it increases over time and manifests itself in a slight shift in the onset time. This illustrates the chaotic nature of the process.

In order to see how the grid resolution affects the system without simultaneously changing the relative size of the damping layers, r_{damp} was set to $1/16$ and $1/8$ instead of $1/10$. This avoids the rounding problem, as the resolutions that are typically used are multiples of eight.

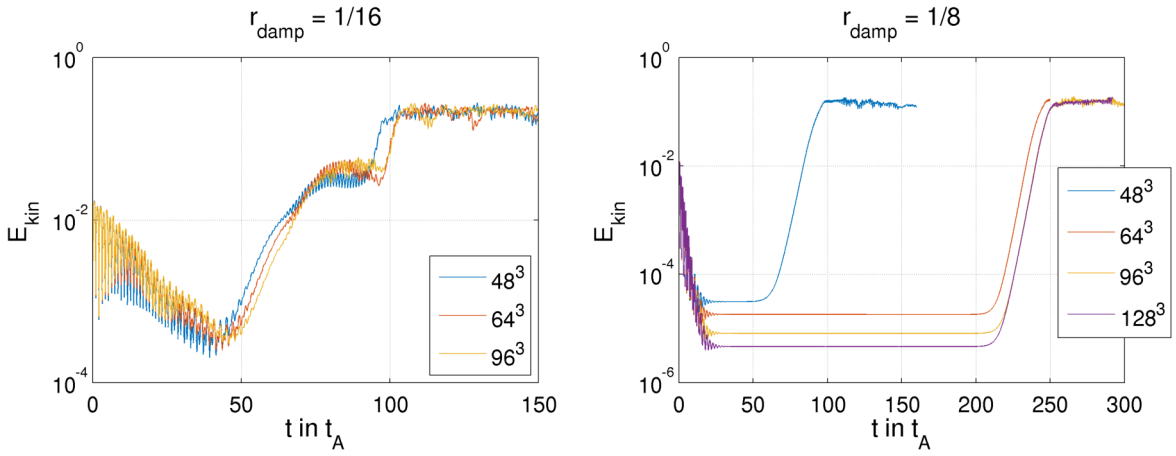

Figure 5.6: Resolution dependency of the kinetic energy evolution: The thickness of the damping layers was set to $r_{damp} = 1/16$ (left) and $r_{damp} = 1/8$ (right). It can be seen that the onset time is shifted to higher values as the resolution increases and converges to a fixed value.

The kinetic energy for different resolutions is shown in figure 5.6 for $r_{damp} = 1/16$ (left) and $r_{damp} = 1/8$ (right). In both cases the onset time is shifted to higher values as the resolution increases. However, in the first case the damping layers are not thick enough for the system to reach a stationary state and the increase in energy is thus not as sudden. In the second case the shift in the onset time is more apparent: while the difference between the resolutions 48^3 and 64^3 is about $150\,t_A$, it becomes quite small for the larger resolutions. It seems to converge to a time of about $220\,t_A$. This shows that after a certain resolution is reached, the resolution does not strongly affect the onset time anymore. Assuming that the numerical resistivity decreases with increasing resolution, this indicates that the onset time is only weakly dependent on the resistivity. This is in line with the theoretical prediction that exponentially small non-ideal effects are sufficient to trigger reconnection. For the following simulations r_{damp} is again set to 0.1, as a larger value such as $1/8$ shifts almost doubles the onset time for high resolutions and thus increases the computation time.

5.2.2 Forcing dependency

Another parameter that strongly influences the system's evolution is the forcing amplitude F_0 introduced in equation (3.26). It affects the stationary energy level, the onset time and the fluctuating energy level, all of which are shifted to higher values as the forcing amplitude increases. The total energy (sum of magnetic and kinetic energy) is shown in figure 5.7a for simulations B1-B5, in which the forcing amplitude is varied from 0.1 to 0.4. The simulation with the largest forcing amplitude of 0.4 had to be aborted, as the forcing caused large fluctuations in the density which lead to numerical difficulties. On the other hand an amplitude lower than 0.1 will have an even higher onset time and lower fluctuating level, so that it is taken as the lower bound.

The total equilibrium energy E_{eq}, averaged over the stationary interval of each simulation, shows a quadratic dependency on the forcing amplitude as is shown in 5.7b, where the data

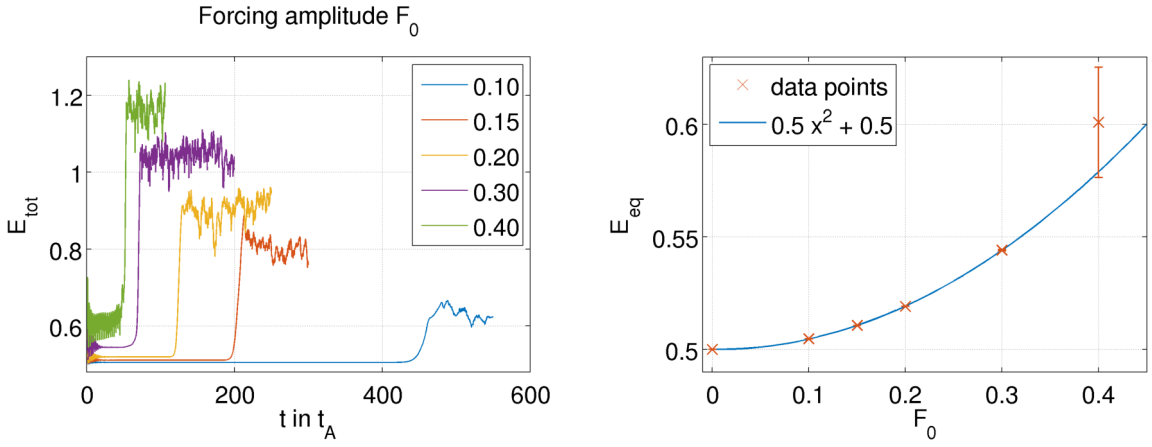

(a) *(b)*

Figure 5.7: Forcing dependency of the total energy evolution: the forcing amplitude was varied (runs B1-B5) between 0.1 and 0.4. An increase in amplitude results in a higher stationary energy level E_{eq}, a higher chaotic energy level and an earlier onset (a). Averaging over the stationary interval gives E_{eq} for each amplitude F_0, with an error given by the standard deviation. The data points were fitted with a quadratic function $ax^2 + bx + c$ (in which the last point was excluded due to the large error), where the parameters were found to be a=0.506, b=0.005 and c=0.500 (b).

points were fitted with a quadratic polynomial. The error corresponds to the standard deviation and is only non-negligible for $F_0 = 0.4$. This is due to the fact that the system does not settle into a stationary state but rather oscillates around a certain energy level. Therefore this data point was not included in the fit, which agrees well with the remaining data points and lies within the error interval of the last one.

The quadratic relation can be explained by considering that the power input P due to the forcing is proportional to $P \sim \boldsymbol{v} \cdot \boldsymbol{F}$. Initially, the velocity field is governed by the applied forcing, such that it is of the order of $v \sim F_0$ and the initial power input approximately scales as $P_{init} \sim F_0^2$. The damped oscillations of the energy in the relaxation phase occur as the system adapts to the forcing and the different forces balance each other out. In the stationary phase the velocity and thus the power input are zero. The equilibrium energy is given by the time integral of the power during the relaxation phase, but is mainly regulated by the initial power input P_{init} that occurs in the first few time steps, as the following oscillations do not put any net power into the system. With this line of reasoning, the equilibrium energy scales with the initial power input $E_{eq} \sim P_{init} \sim F_0^2$, which is consistent with the observed scaling in figure 5.7b.

Both the chaotic energy level and the onset time increase with the forcing amplitude. This behavior is intuitive: An increased forcing amplitude leads to a higher entanglement of the field lines, which are thus more sensitive to perturbations and non-ideal effects, such that the onset happens earlier and more power is put into the system.

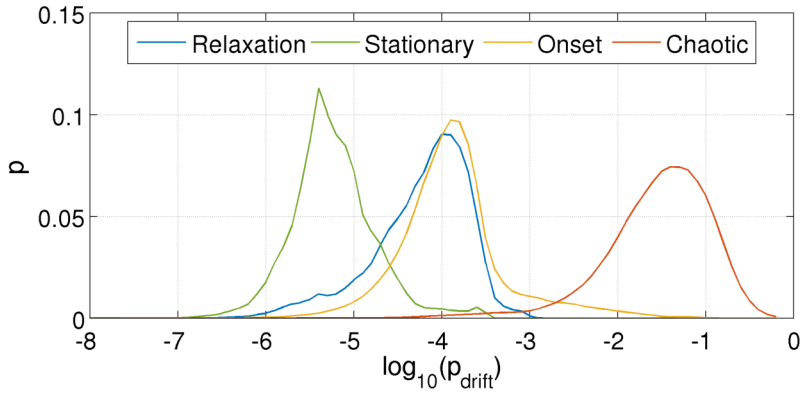

Figure 5.8: Probability density functions of the logarithm of the footpoint drift p_{drift} during the relaxation, stationary, onset and chaotic phase of the system's evolution.

5.3 Chaotic phase

After the analysis of the stationary and onset phase, the chaotic phase is investigated in more detail. It is characterized by strong fluctuations around an increased energy level. Furthermore it is shown in figure 5.3c that the field lines become increasingly chaotic and the footpoints at the top plane no longer coincide with those at the bottom. This change in the footpoint mapping is an indicator for the presence of non-ideal effects, as it is either the result of magnetic diffusion or magnetic reconnection.

The different diagnostic tools introduced in section 4.2 are used to further investigate the field line dynamics in the chaotic phase. A qualitative description is given, in which the effect of resolution and forcing amplitude is again briefly analyzed, after which a statistical analysis of the high resolution run B5 is presented.

5.3.1 Qualitative behavior

As explained in section 4.2.1 the footpoint drift, p_{drift}, and the associated velocity, v_{fp}, are important quantities, which are useful in identifying potential reconnection events. From the distributions of the footpoint drift during the various phases of the system evolution shown in figure 5.8, it can be seen that during the chaotic phase the footpoint drift shows an increase of about four orders of magnitude compared to the stationary phase. The distributions for the relaxation and onset phase are comparable to each other and the average values are still about three orders of magnitude below that of the chaotic phase. The distribution of the onset phase overlaps with both the stationary and chaotic phase and can thus be understood as an intermediate state, in which a few field lines start undergoing changes in their mapping, thereby disrupting the stationary state. Once this occurs, the force balance is no longer given and the forcing puts energy into the system, which in turn leads to more and larger footpoint drifts during the chaotic phase. For reference, the maximal possible drift is given by $\sqrt{0.5}$ or about -0.15 on the logarithmic scale, which shows that the drifts in the chaotic phase are of a significant magnitude. This quantitatively supports the previous assessment that reconnection

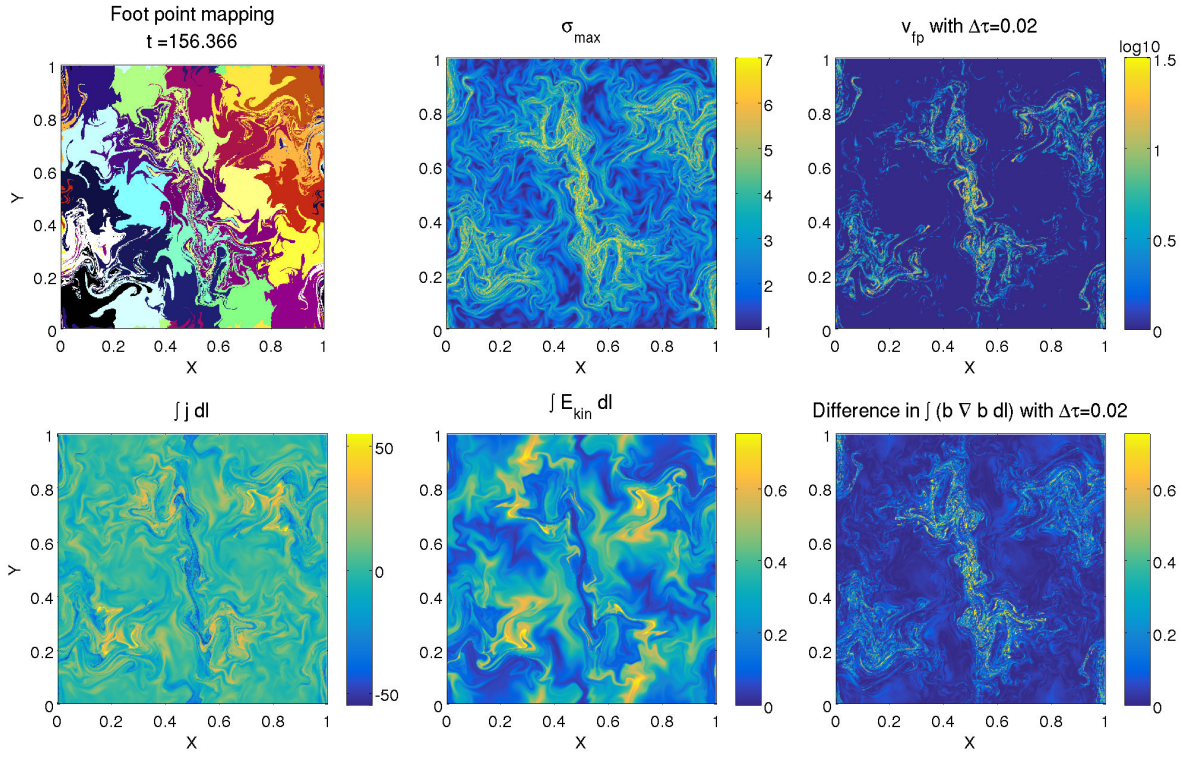

Figure 5.9: Snapshot from run B5 during the chaotic phase: The first row shows the footpoint mapping, the maximum exponentiation number and the footpoint velocity. The second row shows the integrated current density, the integrated kinetic energy and the temporal changes of the integrated magnetic tension term. Both the footpoint velocity and the difference in magnetic tension were computed from two consecutive snapshots separated by $\Delta\tau = 0.02 t_A$.

triggers the onset and occurs constantly in the chaotic phase. However, the footpoint drifts could also be caused by field line diffusion, such that further investigation is necessary.

The various diagnostics can be used to better evaluate what is happening in the chaotic phase. A snapshot from run B5 during the chaotic phase shows that a strong distortion of the footpoint mapping is accompanied by a locally enhanced exponentiation number, footpoint velocity and integrated current density, all of which exhibit a similar spatial structure, see figure 5.9. The original checkerboard pattern can still be recognized in the deformed footpoint mapping, which shows an overall distortion of the pattern as well as thin long structures extending from their original regions, resulting in a complex structure. The exponentiation number reaches large values with a maximum of about 13. The footpoint velocity was computed from two snapshots separated by $\Delta\tau = 0.02 t_A$, and reaches values over an order of magnitude above the Alfvén velocity.

The integrated kinetic energy has a complex spatial structure as well, which does not directly coincide with the remaining ones. Nevertheless, it can be seen that regions of high kinetic energy are tendentially located around or close to regions in which the other quantities are strongly enhanced. This indicates that magnetic energy is converted to kinetic energy for example by a reconnection process. Finally, the magnetic tension term $\boldsymbol{B}\boldsymbol{\nabla}\boldsymbol{B}$ was integrated along the field lines and the difference between two subsequent frames was computed. As

before, it shows a very similar structure to the previous quantities. A change in the footpoint mapping of a field line is therefore correlated with a change in the magnetic tension along that field line. This is intuitive as the magnetic tension measures the curvature of the field lines and a change in the mapping is likely to result in a change in the curvature.

Note that figure 5.9 only shows a single snapshot of the structure, which is changing its overall shape on a time scale of the Alfvén transit time t_A (e.g. compare to figure 5.10, which shows a different snapshot of run B5 in the third column). Individual field lines on the other hand change their footpoint positions significantly on sub-Alfvénic time scales ($\sim 0.01 t_A$) as can be seen by the large footpoint velocities. The accumulation of these quick changes together with more gradual changes, e.g. through magnetic diffusion, then lead to changes of the large-scale structure.

Resolution dependency

Snapshots of the footpoint mapping and the exponentiation number are shown for resolutions $N = 64, 128, 256$ (runs B2, B4 and B5) in figure 5.10. In all cases, the distortion of the footpoint mapping is related to a similar structure in the exponentiation number. A higher resolution results in larger values of the exponentiation number and a more complex structure. While for $N = 64$ there are mainly two pronounced regions of high exponentiation number (when considering that the boundaries are periodic) that coincide with large deviations from the

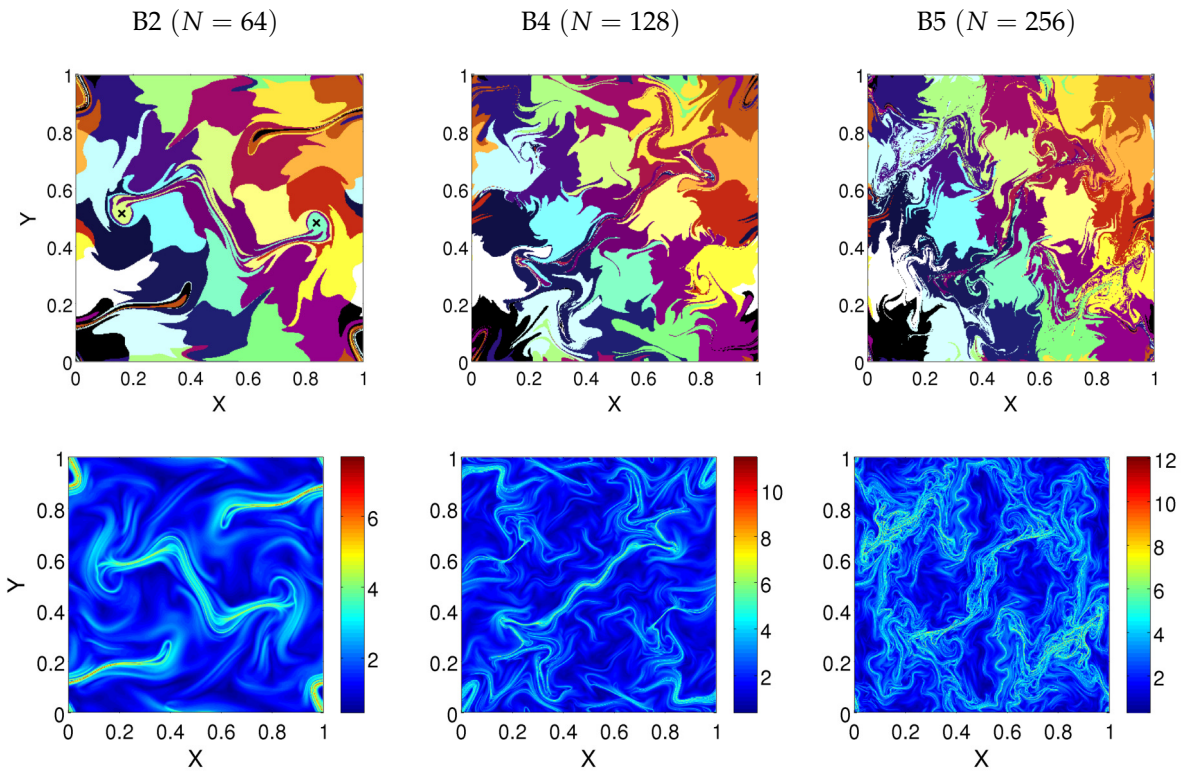

Figure 5.10: Snapshots of the footpoint mapping (a) and exponentiation number (b) for different resolutions (runs B2, B4 and B5).

original mapping, for $N = 256$ no clear distinct regions are discernible. Instead there exist many thin and entangled regions of enhanced exponentiation.

For the following statistical analysis, the highest resolution run B5 will be used. However, for the qualitative understanding of the process, the footpoint mapping of the low resolution run B2 is more accessible: The regions marked by the different colors of the initial checkerboard pattern are distorted but generally remain connected. However, the two circles at the end of the central z-shaped structure for instance (marked by black crosses in figure 5.10), are largely separated from their original region. By comparing multiple consecutive frames it can be seen that they do not separate and gradually move away from their colored region but appear rapidly compared to the general distorting motion. This is comparable to the sudden changes in the footpoint mapping in regions of high exponentiation observed in [17], in which a similar numerical experiment was carried out.

Forcing dependency

Similarly, the influence of the forcing amplitude on the field line dynamics during the chaotic phase is investigated for the runs C1-C5. For the lowest amplitude (run C1) the footpoint mapping shows only slight deviations from the original pattern and the exponentiation number is comparatively low, see figure 5.11. An increase in the forcing amplitude leads to higher exponentiation numbers. This is to be expected as the forcing amplitude controls the plasma velocity and thus the entanglement of field lines, which is measured by the exponentiation

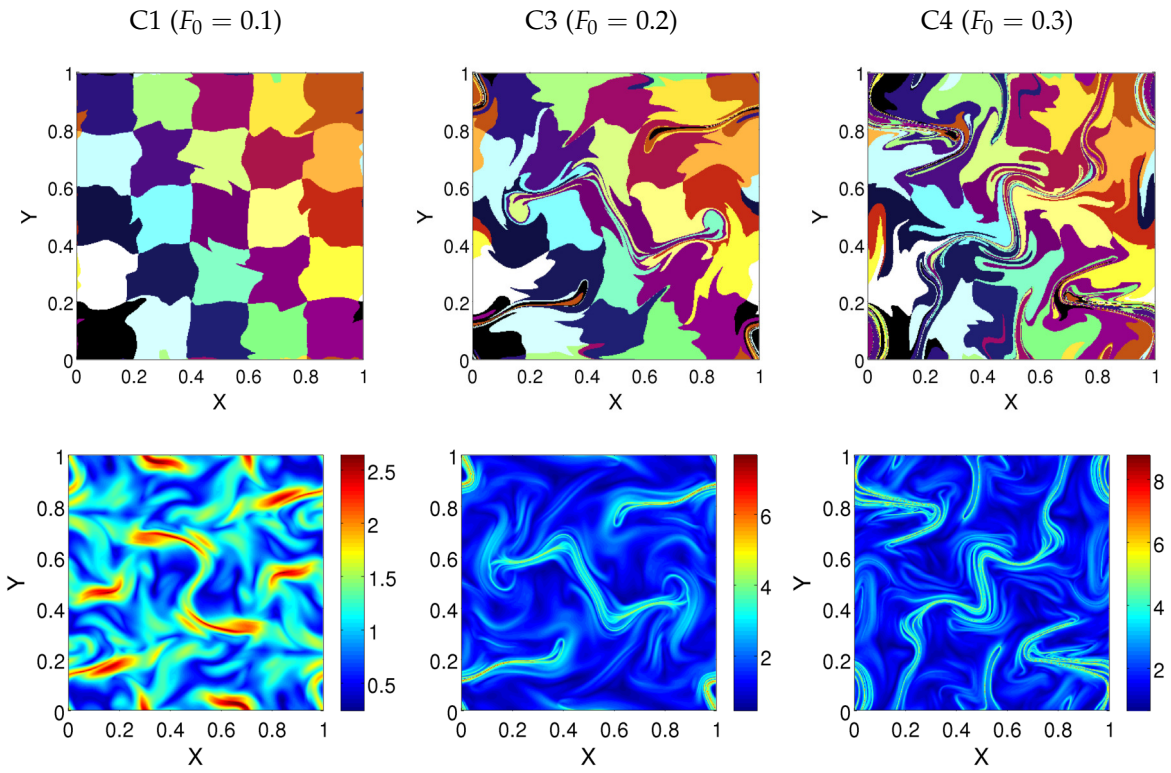

Figure 5.11: Snapshots of the footpoint mapping (top row) and exponentiation number (bottom row) for different forcing amplitudes (runs C1, C3 and C4).

number. Simultaneously, the deformation of the footpoint mapping increases visibly, which suggests that indeed the exponentiation number is related to the changes in footpoint mapping and thus to the occurrence of reconnection events, assuming that changes in the mapping are a signature of reconnection.

As before only a single snapshot is shown in figure 5.11 for each forcing amplitude, but the time evolution of the different diagnostic quantities is also of interest. As described in the previous section, the energy in the chaotic phase fluctuates around a certain level. The same is true for the exponentiation number, footpoint drift, integrated current density and integrated kinetic energy. The maximum value of these quantities taken over all field lines is shown in figure 5.12a for runs C1-C4, where the time axis was shifted by the respective onset times. All four quantities show a sharp increase during the onset, followed by fluctuations

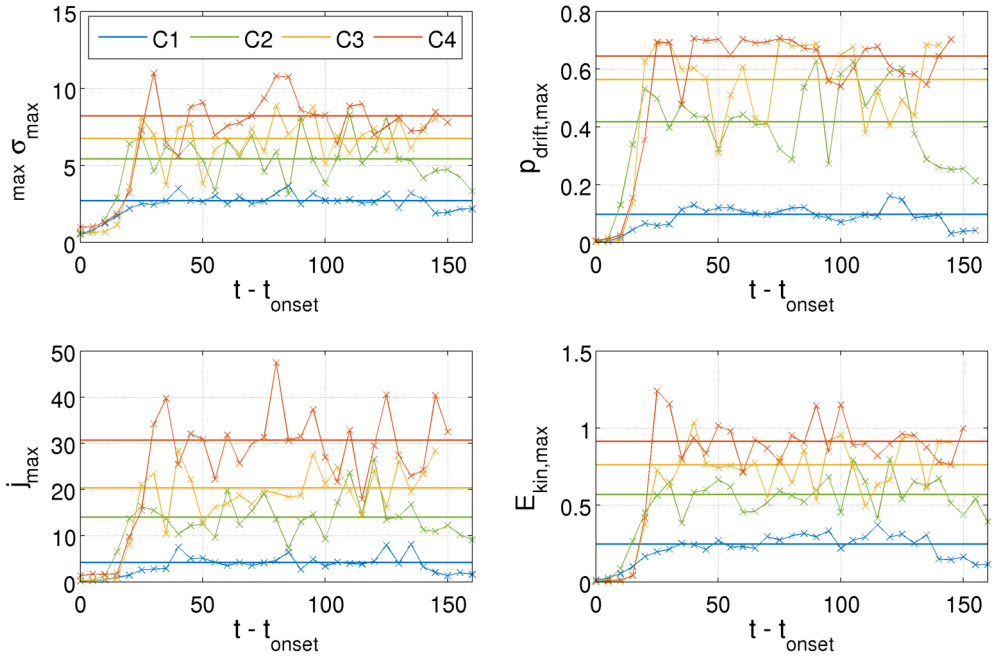

(a)

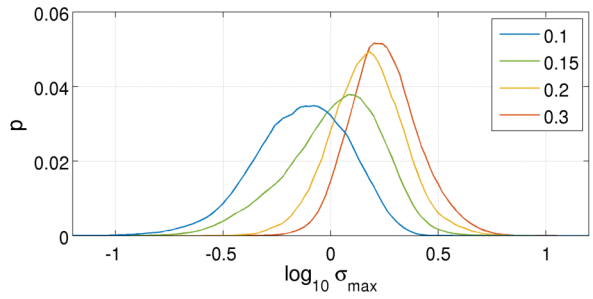

(b)

Figure 5.12: Forcing amplitude dependency of the diagnostic quantities for the simulation runs C1-C4: (a) Time evolution of exponentiation number, footpoint drift, integrated current and integrated kinetic energy, where in all cases the maximum over all field lines was taken. The horizontal lines mark the average value computed from the points after the increase (b). The probability density functions of the logarithm of the exponentiation number.

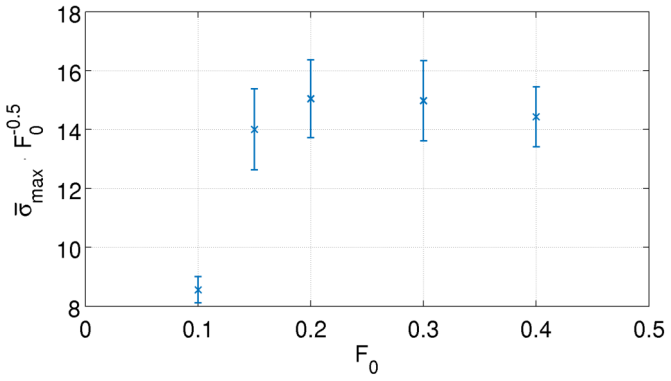

Figure 5.13: Scaling of the time-averaged maximum exponentiation number $\overline{\sigma}_{max}$ with the forcing amplitude F_0(simulations C1-C5): The values were compensated with $1/\sqrt{F_0}$ to verify the predicted scaling of $\overline{\sigma}_{max} \sim \sqrt{F_0}$. The error bars correspond to the standard deviation.

around a constant value. Additionally, the probability density function of the logarithm of the exponentiation number of all field lines is shown in figure 5.12b. It approximately has the shape of a normal distribution, which means that the exponentiation number follows a log-normal distribution. The mean value of $\log_{10} \sigma_{max}$ is shifted towards higher values for increasing forcing amplitudes.

This data can be used to investigate the scaling of the maximum exponentiation number with the forcing amplitude. As described in section 2.2.1 the scaling is estimated to be

$$\sigma \sim \sqrt{F_0}.$$

It is tested using the maximum exponentiation number $\max(\sigma_{max})$ over all field lines averaged over time in the chaotic phase for runs C1-C5. This gives a mean value $\overline{\sigma}_{max}$, shown as horizontal lines in figure 5.12a. Compensating these values of $\overline{\sigma}_{max}(F_0)$ with $1/\sqrt{F_0}$ should result in a horizontal line if the predicted scaling is indeed correct. This is shown in figure 5.13, where the error bars are given by the standard deviation of the averaged maximum exponentiation number. It can be seen that the values lie on a horizontal line within their error intervals with the exception of the first data point, which lies significantly lower than the others. It is possible that this is due to the fact that the lowest forcing amplitude lies right at the boundary of what is needed to observe the onset and the chaotic phase at all. This tendency can also be seen in the energy evolution of this run in figure 5.7a, where the shift in onset time is relatively large compared to the other runs. The estimated scaling thus might only be valid once a certain forcing amplitude is exceeded. Furthermore, the statistics could be improved by using more frames in the time series, from which the average $\overline{\sigma}_{max}(F_0)$ is computed.

5.3.2 Statistical analysis of run B5

Instead of considering only single snapshots or averaged quantities, a statistical analysis of the highest resolution run B5 is carried out to quantitatively test the relation of exponentiation number and changes in the footpoint mapping. These are measured through the footpoint velocity, which is used as a proxy for potential reconnection events. The correlation of these two

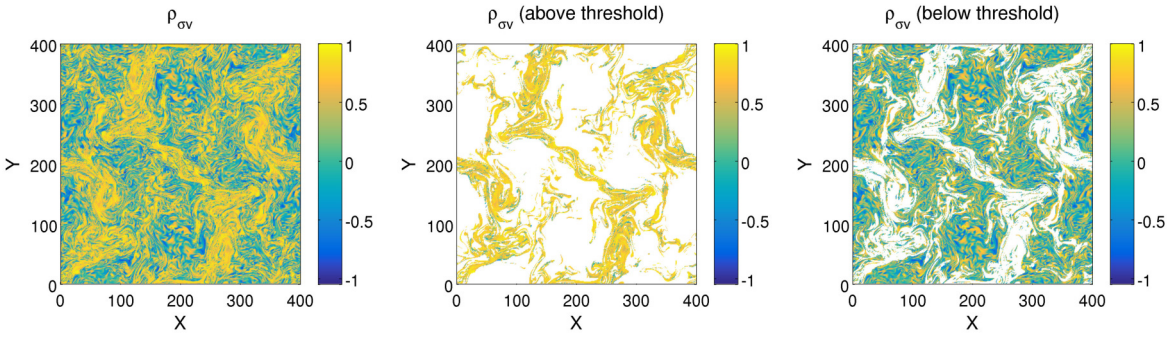

Figure 5.14: Correlation coefficient $\rho_{\sigma v}$ of the exponentiation number σ_{max} and the footpoint velocity v_{fp} computed for each field line (left). A time series consisting of a hundred consecutive frames with a time step of $\Delta\tau = 0.001\, t_A$ was used. A threshold for the maximum footpoint velocity was used to select field lines, which underwent potential reconnection events. The correlation of the selected (center) and the remaining (right) field lines are shown.

quantities is assessed through their correlation coefficients, introduced in section 4.2.2. A typical length scale of the reconnection regions is obtained from the distribution of the footpoint velocity. Furthermore, the average event duration is estimated using the autocorrelation of the footpoint velocities.

Correlation of exponentiation number and footpoint velocity

The relation between the exponentiation number σ_{max} and the footpoint velocity v_{fp} is evaluated via the correlation coefficient $\rho_{\sigma v}$ introduced in section 4.2.2. In fact, both quantities follow a log-normal distribution and thus the logarithm of both quantities is used to compute $\rho_{\sigma v}$. This is done separately for each of the 400×400 field lines using time series consisting of 100 consecutive frames with a time step of $\Delta\tau = 0.001\, t_A$, for a time interval of $0.1\, t_A$. A total of ten such time series are considered, in order to investigate the correlation at different points in time. They are spaced apart by $1\, t_A$ as the overall structure changes on this time scale, such that they can be considered independent of each other.

The correlation coefficient for each field line is shown exemplary for one of the samples in figure 5.14 (left). A structure of high correlation $\gtrsim 0.5$ stands out against a noisy background across the whole range of values. A majority of the field lines actually does not undergo significant changes in their footpoint positions during the selected time span and is thus not of interest. Instead, field lines that contain a peak in the time series of their footpoint velocity should be selected, as these are the ones that experience potential reconnection events. The selection is done by setting the following threshold for the maximum of the footpoint velocity $v_{ij}(t)$ of the field line indexed by (i, j):

$$\max(v_{ij}(t)) \geq 2\overline{v}_{fp}. \tag{5.1}$$

Here $\overline{v}_{fp}$ denotes the mean value of the footpoint velocity distribution, which takes into account the velocities of all field lines for each frame in the respective time series. It takes on values between $0.7\, v_A$ and $1.8\, v_A$ for all ten samples.

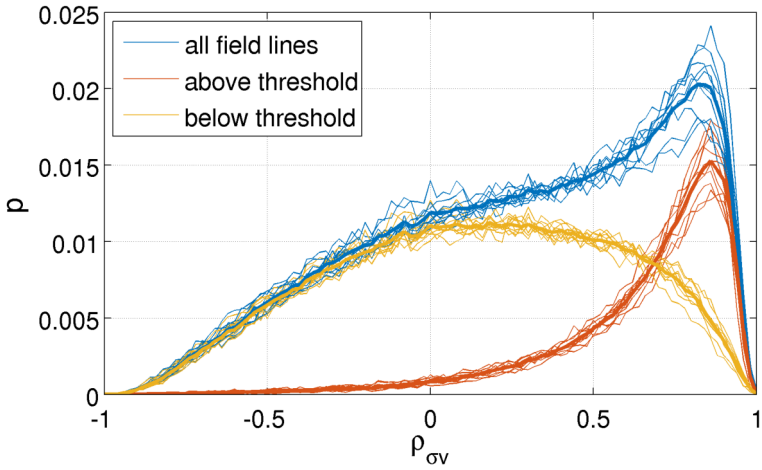

Figure 5.15: Probability density function of the correlation coefficients $\rho_{\sigma v}$: The field lines are separated into two groups, depending on whether their maximum footpoint velocity exceeds a certain threshold (equation (5.1)). The correlation coefficients of all field lines and of the separate groups are shown for each of the ten samples (thin lines) as well as the average for each group (thick lines).

As discussed in section 4.2.1 different measures for the central tendency of a distribution exist, that could be used to define a threshold. However, using the median or the mode of the distribution would have lowered the threshold such that almost all field lines would have been selected, as both were significantly smaller than the mean value. The threshold was set for the maximum velocity such that field lines with a sharp peak but otherwise negligible footpoint velocity are still selected.

The correlation coefficients of the selected and remaining field lines are shown in figure 5.14 (center and right, respectively). It can be seen that the structure of comparatively high correlation was effectively selected, while the coefficients of the remaining field lines seem to be distributed randomly, which indicates that the chosen threshold was indeed suitable. The shapes of the probability density functions of the correlation coefficients shown in figure 5.15 support this assessment. All ten samples were treated separately (thin lines) and have similar distributions; their averages are given by the thicker lines. The field lines that did not fulfill the criterion are distributed over the whole range of coefficients, which indicates that the two quantities are independent of each other and any positive or negative linear correlation occurred coincidentally. There is a slight positive skew, that could be caused by the fact that field lines with a less pronounced peak were not selected and could probably be reduced by modifying the threshold or adding additional selection criteria. On the other hand, the curves for the selected field lines have a clear maximum at $\rho_{\sigma v} \approx 0.86$ and decrease rapidly towards lower values, such that one has $p(\rho_{\sigma v} \geq 0.5) \approx 0.78$. This verifies that there is a strong correlation between the footpoint velocity and exponentiation number for these field lines and thus supports the theoretical prediction.

An example of the time series of the correlated quantities, $\log_{10} \sigma_{max}$ and $\log_{10} v_{fp}$, of a selected field line with a correlation coefficient of $\rho_{\sigma v} = 0.88$ is given in figure 5.16. Additionally, the footpoint velocity is shown as it illustrates that distinct events of greatly enhanced velocities have occurred. Some of the peaks are broadened and seem to consist of several peaks, which

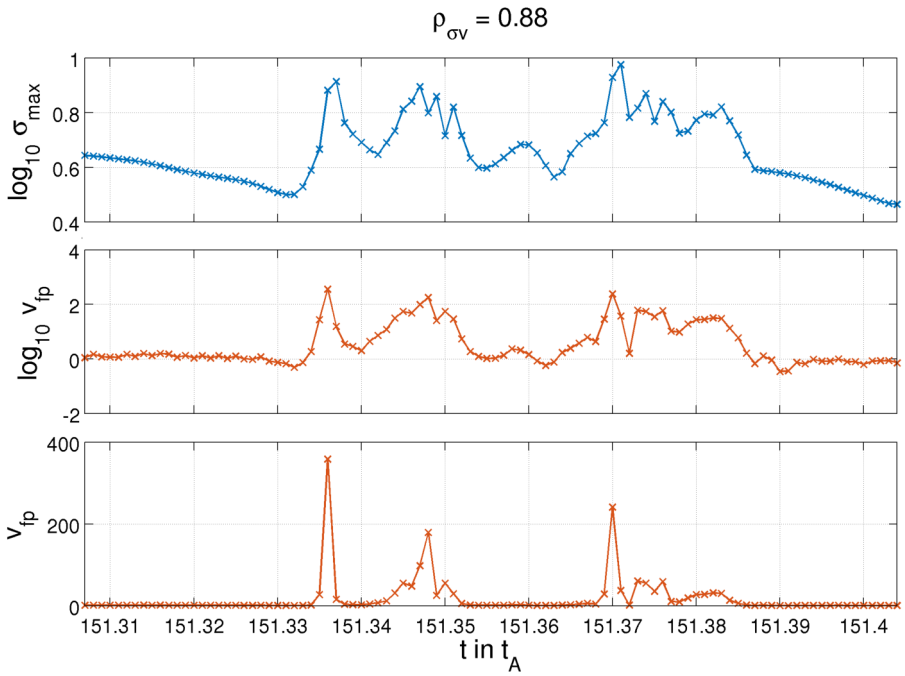

Figure 5.16: Time series of the logarithm of the exponentiation number, the logarithm of the footpoint velocity and the footpoint velocity for a single field line. The correlation coefficient between the first two quantities is given by $\rho_{\sigma v} = 0.88$.

could not be fully resolved with the chosen time step. A higher time resolution could thus lead to even more pronounced peaks and higher correlation coefficients. Nevertheless, this clearly shows that the footpoint positions can rapidly and abruptly change with velocities of the order of $\sim 10^2\, v_A$. This velocity, though, does not correspond to a material plasma displacement and should not be interpreted in this way. It represents a measure of footpoint distance between reconnecting field lines.

Estimation of the event duration

Each occurrence of high footpoint velocity is interpreted as a potential reconnection event. The event duration τ_{event} of these events can be estimated from the autocorrelation of the footpoint velocity as explained in section 4.2.2. It is computed for each of the selected field lines and the ten samples. The resulting probability density function is shown in figure 5.17. The duration can only attain discrete values prescribed by the time step $\Delta\tau$ and is limited by the length of the time series $0.1\, t_A$, but in practice $\tau_{event} < 0.04\, t_A$. The mode of the distribution lies at $0.003\, t_A$ after which the probability density decays approximately exponentially. The median and the mean value are given by $0.006\, t_A$ and $0.008\, t_A$, respectively. The typical time scale of the events is thus on the order of $10^{-3}\, t_A$.

An example for such an event is given in figure 5.18, where four frames of two field line bundles are shown in the top view of the x-y plane. The radius of the field line bundles is set according to the typical length scale of the system, which was estimated to be $\overline{v}_{fp}\Delta\tau \approx 0.0015$. It can be seen that the field lines in the bundles successively undergo the same motion. First

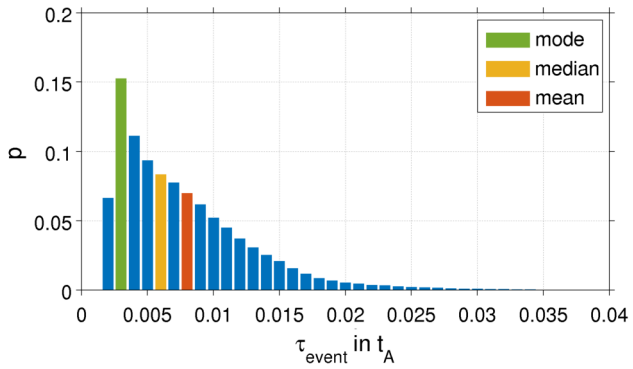

Figure 5.17: Probability density of the event duration of all selected field lines for all ten samples. It was estimated via the autocorrelation of the footpoint velocity.

two field lines of the opposite bundles approach each other, before apparently flipping positions in what appears to be a spontaneous reconnection process. This occurs on a time scale of $0.04\,t_A$ for a single pair of field lines (see the highlighted field lines in the right frames).

In summary, the presented results suggest that the observed changes in the footpoint mapping are caused by reconnection, as they occur abruptly on very short time scales. Furthermore, the footpoint velocity is strongly correlated with the exponentiation number for selected field lines that undergo such an event. All of this is consistent with the theory that an entanglement of field lines causes an exponential sensitivity to non-ideal effects.

These results are comparable to those presented in [18], where three-dimensional reconnection was discussed specifically with regard to eruptive flares. MHD simulations of a flux rope were carried out with similar line-tied boundary conditions. The changes in footpoint connectivity are discussed with respect to the so-called squashing factor Q, which is similar to the exponentiation number and is often discussed in relation to quasi-separatrix layers (QSLs) [13, 32]. In sections 3.3 and 4.1 the time series of the footpoint velocity of a single field line is investigated and shown to be highly correlated with the squashing factor Q and

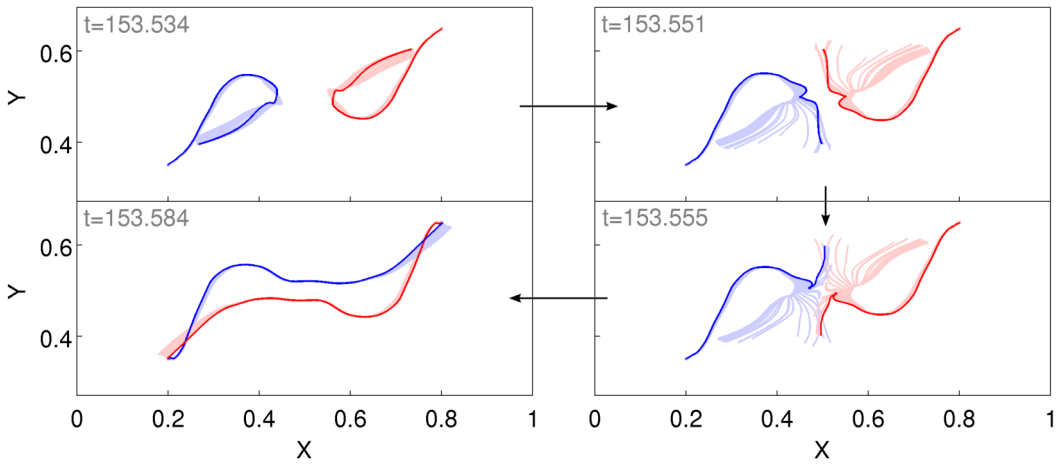

Figure 5.18: Snapshots of two field line bundles successively reconnecting pairwise (top view of the x-y plane). A pair of reconnecting field lines is highlighted.

associated quantities. As the motion of the field lines observed is super-Alfvénic, it is classified as *slip-running reconnection*. This phenomenon is proposed to fill the gap between abrupt reconnection and slow magnetic diffusion, as in three dimensions no clear line can be drawn between those two processes [4].

This line of reasoning supports the argument, that the events observed in this work are indeed a form of reconnection. Furthermore, the distinction between reconnection and diffusion is discussed in [17], where changes in the footpoint mapping that occurred rapidly were classified as reconnection, as opposed to footpoint drifts that occurred gradually due to field line diffusion. This is similar to what is observed in this work, where the overall structure is distorted on a much slower time scale than certain individual field lines, that experience very large footpoint velocities.

6 Summary and Outlook

The aim of this thesis is to investigate the topology-driven reconnection model described in chapter 2, in which a reconnection trigger is given by the exponential sensitivity to non-ideal effects of highly entangled field lines. This model is accessible to numerical investigation through a simple numerical setup, in which an initially uniform magnetic field is driven to a high degree of entanglement by an externally applied forcing. The footpoints of the field lines are fixed at the boundary through no-slip boundary conditions, which set the velocity at these boundaries to zero. This makes it possible to observe reconnection events through changes in the footpoint mapping. The exponentiation number is introduced as a quantity to measure the separation of neighboring field lines and characterize the degree of entanglement. It can be compared to the footpoint velocity in order to verify the theory.

The simulations are performed using a fourth-order accurate CWENO finite-volume scheme presented in chapter 3, which solves the ideal MHD equations. The resistivity required for reconnection to occur arises due to numerical dissipation and is not controllable in this setup. The reconnection model requires the implementation of specific boundary conditions and an external forcing to drive the field lines to entanglement. Additionally, damping layers are included to damp perturbations caused by Alfvén waves. It is found that of two tested ways of setting the boundary condition for the velocity, one of them preserves the fourth-order accuracy of the numerical scheme.

The various simulation runs listed in table 4.1 are used to investigate the effect of the damping layers (set A), the forcing amplitude (set B) and the grid resolution (set C) on the system's evolution. The time frames produced by the simulations are used to integrate an array of 400×400 field lines, along which various diagnostic quantities such as the exponentiation number and the footpoint velocity are computed, as described in chapter 4.

The results are presented and discussed in chapter 5. The time evolution of the system is investigated based on the mean magnetic and kinetic energy for different damping strengths. For the strongest damping, the evolution is divided into four phases: In the first phase the interplay of the external forcing with the remaining forces causes the system to relax into a stationary state, in which the magnetic field lines settle into a twisted state and the plasma velocity becomes zero. A sudden increase in energy in the onset phase, which is presumably triggered by reconnection and disrupts the force-balance of the stationary phase, is followed by the chaotic phase, in which the energy fluctuates around an increased energy level. The stationary phase and the nature of the onset is further investigated and discussed in relation to the resolution and forcing amplitude in section 5.2.

Furthermore it is found that during the onset and especially the chaotic phase, drastically increased footpoint drifts occur, supporting the argument that the onset is triggered by reconnection. A snapshot of the various diagnostic quantities during the chaotic phase is shown for an array of 400×400 field lines and it is found that a distortion of the footpoint mapping is accompanied by locally enhanced exponentiation number, footpoint velocity and parallel current density, all of which exhibit the same spatial structure, as shown in section 5.3 and presented in [23].

For the highest resolution run B5 ($N = 256$) the correlation of the exponentiation number, σ_{max}, and the footpoint velocity, v_{fp}, is studied, as the former measures the entanglement and the latter is a measure of reconnection events. The correlation is evaluated via a correlation coefficient, $\rho_{\sigma v}$, computed from the time series of $\log(\sigma_{max})$ and $\log(v_{fp})$ for each field line. A threshold is used to select the field lines that experience a significant foot point velocity during the time period under investigation and it is found that there is a strong correlation for these selected field lines, as shown in figure 5.15, which is consistent with the theory. Individual events are shown to occur abruptly on short time scales of $\tau_{event} \sim 0.001\, t_A$, which suggests that it is indeed reconnection that causes the motion of the field lines.

In the future, this reconnection model could be further investigated by extending the numerical code to include physical resistivity. This has the advantage that the magnitude of the resistive effects is known and controllable. It can then be varied in order to see its effect on the system's evolution and used for the computation of the reconnection rate from the parallel electric field. Furthermore, the force balance in the stationary state and its disruption could be investigated in more detail, e.g. by studying the scaling of the onset times, energy levels and the steepness of the energy increase with the exponentiation number, which in turn depends on the damping and forcing amplitudes. The analysis of the chaotic phase for run B5 could be done for other runs, in order to see how the different parameters influence the found results. It could be further extended by investigating the number of events selected by the threshold and comparing this to the reconnection rates, once these can be computed. Additionally, other parameters of the system could be varied, e.g. the dimensions of the computational domain or the forcing that is used to drive the system. Finally, this reconnection model could be applied to altogether different systems with more complex initial conditions, to see if the obtained results can be generalized to other systems.

Acknowledgments

Firstly, I would like to thank Prof. Dr. Müller for welcoming me into his group and supervising this project. Thanks to his time and interest in this work I was able to learn a lot about numerics, physics and how to be a cool researcher.

I would also like to thank Prof. Dr. Breitschwerdt for his interest in my project in particular during the midterm presentation and for reviewing this work.

I much enjoyed working in the plasma-astrophysics group thanks to all the great people and the friendly atmosphere. In particular, I would like to thank Jean-Mathieu for his constant enthusiasm and support throughout this year and for always taking the time to answer my questions.

Finally, I want to express my gratitude toward my friends and family for their love and support throughout my studies. Special thanks to my parents for always believing in me, to Sarah for our conversations about work and everything else, and to Phill for being by my side every step of the way.

7 Bibliography

[1] Alfvén, H. Existence of electromagnetic-hydrodynamic waves. *Nature 150*, 3805 (1942), 405.

[2] Anderson, E., Bai, Z., Bischof, C., Blackford, S., Demmel, J., Dongarra, J., Du Croz, J., Greenbaum, A., Hammarling, S., McKenney, A., and Sorensen, D. *LAPACK Users' Guide*, third ed. Society for Industrial and Applied Mathematics, Philadelphia, PA, 1999.

[3] Atkinson, K. E. *An introduction to numerical analysis*. John Wiley & Sons, 2008.

[4] Aulanier, G., Pariat, E., Demoulin, P., and Devore, C. Slip-running reconnection in quasi-separatrix layers. *Solar Physics 238*, 2 (2006), 347–376.

[5] Baumjohann, W., and Treumann, R. A. *Basic space plasma physics*. World Scientific Publishing Company, 2012.

[6] Biskamp, D. *Nonlinear magnetohydrodynamics*, vol. 1. Cambridge University Press, 1997.

[7] Biskamp, D. *Magnetohydrodynamic turbulence*. Cambridge University Press, 2003.

[8] Boozer, A. H. Magnetic reconnection in space. *Physics of Plasmas 19*, 9 (2012), 092902.

[9] Boozer, A. H. Separation of magnetic field lines. *Physics of Plasmas 19*, 11 (2012), 112901.

[10] Boozer, A. H. Model of magnetic reconnection in space and astrophysical plasmas. *Physics of Plasmas 20*, 3 (2013), 032903.

[11] Chatfield, C. *Time-series forecasting*. Chapman and Hall/CRC, 2000.

[12] Dagum, L., and Menon, R. OpenMP: An industry-standard API for shared-memory programming. *Computing in Science & Engineering*, 1 (1998), 46–55.

[13] Demoulin, P., Bagala, L., Mandrini, C., Henoux, J.-C., and Rovira, M. Quasi-separatrix layers in solar flares. II. Observed magnetic configurations. *Astronomy and Astrophysics 325* (1997), 305–317.

[14] Evans, C. R., and Hawley, J. F. Simulation of magnetohydrodynamic flows-a constrained transport method. *The Astrophysical Journal 332* (1988), 659–677.

[15] Hesse, M., Forbes, T. G., and Birn, J. On the relation between reconnected magnetic flux and parallel electric fields in the solar corona. *The Astrophysical Journal 631*, 2 (2005), 1227.

[16] Hesse, M., and Schindler, K. A theoretical foundation of general magnetic reconnection. *Journal of Geophysical Research: Space Physics 93*, A6 (1988), 5559–5567.

[17] Huang, Y.-M., Bhattacharjee, A., and Boozer, A. H. Rapid change of field line connectivity and reconnection in stochastic magnetic fields. *The Astrophysical Journal 793*, 2 (2014), 106.

[18] Janvier, M., Aulanier, G., Pariat, E., and Demoulin, P. The standard flare model in three dimensions-III. Slip-running reconnection properties. *Astronomy & Astrophysics 555* (2013), A77.

[19] Ketcheson, D. I. Highly efficient strong stability-preserving Runge–Kutta methods with low-storage implementations. *SIAM Journal on Scientific Computing 30*, 4 (2008), 2113–2136.

[20] Lapenta, G., and Lazarian, A. Achieving fast reconnection in resistive MHD models via turbulent means. *Nonlinear Processes in Geophysics 19* (2012), 251–263.

[21] Lekien, F., and Marsden, J. Tricubic interpolation in three dimensions. *International Journal for Numerical Methods in Engineering 63*, 3 (2005), 455–471.

[22] Lewy, H., Friedrichs, K., and Courant, R. Über die partiellen Differenzengleichungen der mathematischen Physik. *Mathematische Annalen 100* (1928), 32–74.

[23] Mäusle, R., Teissier, J.-M., and Müller, W.-C. Investigation of topology-driven magnetic reconnection with CWENO finite volume numerics. Poster presented at the DPG Spring meeting 2019, Munich, Germany.

[24] Parker, E. N. Sweet's mechanism for merging magnetic fields in conducting fluids. *Journal of Geophysical Research 62*, 4 (1957), 509–520.

[25] Pontin, D. Three-dimensional magnetic reconnection regimes: A review. *Advances in Space Research 47*, 9 (2011), 1508–1522.

[26] Pontin, D., Wilmot-Smith, A., Hornig, G., and Galsgaard, K. Dynamics of braided coronal loops-II. Cascade to multiple small-scale reconnection events. *Astronomy & Astrophysics 525* (2011), A57.

[27] Priest, E., and Forbes, T. Magnetic reconnection, 2000.

[28] Priest, E., Hornig, G., and Pontin, D. On the nature of three-dimensional magnetic reconnection. *Journal of Geophysical Research: Space Physics 108*, A7 (2003).

[29] Snir, M., Gropp, W., Otto, S., Huss-Lederman, S., Dongarra, J., and Walker, D. *MPI–the Complete Reference: The MPI core*, vol. 1. MIT press, 1998.

[30] Sornette, D. *Critical phenomena in natural sciences: chaos, fractals, self-organization and disorder: concepts and tools*. Springer Science & Business Media, 2006.

[31] Sweet, P. A. 14. The neutral point theory of solar flares. In *Symposium-International Astronomical Union* (1958), vol. 6, Cambridge University Press, pp. 123–134.

[32] Titov, V. S. Generalized squashing factors for covariant description of magnetic connectivity in the solar corona. *The Astrophysical Journal 660*, 1 (2007), 863.

[33] Trefethen, L. N., and Bau III, D. *Numerical linear algebra*, vol. 50. Society for Industrial and Applied Mathematics, 1997.

[34] Verma, P. S., and Müller, W.-C. Higher order finite volume central schemes for multi-dimensional hyperbolic problems. *Journal of Scientific Computing 75*, 2 (2018), 941–969.

[35] Verma, P. S., Teissier, J.-M., Henze, O., and Müller, W.-C. Fourth-order accurate finite-volume CWENO scheme for astrophysical MHD problems. *Monthly Notices of the Royal Astronomical Society 482*, 1 (2018), 416–437.